



Variability in the Energetic Electron Bombardment of Ganymede

Key Points:

- Ganymede's plasma interaction causes bombardment of energetic electrons to be highly inhomogeneous across the polar and equatorial surface
- The polar electron flux exceeds the ion flux by an order of magnitude; the equatorial flux from electrons above 40 MeV compares to ion fluxes
- The trailing anti-Jovian equator receives the least flux over geologic timescales; the trailing surface near the OCFB receives the most

Supporting Information:

- Supporting Information S1
- Figure S1
- Figure S2
- Figure S3

Correspondence to:

L. Liuzzo,
liuzzo@berkeley.edu

Citation:

Liuzzo, L., Poppe, A. R., Paranicas, C., Nénon, Q., Fatemi, S., & Simon, S. (2020). Variability in the energetic electron bombardment of Ganymede. *Journal of Geophysical Research: Space Physics*, 125, e2020JA028347. <https://doi.org/10.1029/2020JA028347>

Received 12 JUN 2020

Accepted 28 AUG 2020

Accepted article online 2 SEP 2020

Lucas Liuzzo¹, Andrew R. Poppe¹, Christopher Paranicas², Quentin Nénon¹, Shahab Fatemi^{3,4}, and Sven Simon⁵

¹Space Sciences Laboratory, University of California, Berkeley, CA, USA, ²The Johns Hopkins University Applied Physics Laboratory, Laurel, MD, USA, ³Swedish Institute of Space Physics, Kiruna, Sweden, ⁴Department of Physics, Umeå University, Umeå, Sweden, ⁵School of Earth and Atmospheric Sciences, Georgia Institute of Technology, Atlanta, GA, USA

Abstract This study examines the bombardment of energetic magnetospheric electrons onto Ganymede as a function of Jovian magnetic latitude. We use the output from a three-dimensional, hybrid model to constrain features of the electromagnetic environment during the G1, G8, and G28 Galileo encounters when Ganymede was located far above, within, or far below Jupiter's magnetospheric current sheet, respectively. To quantify electron fluxes, we use a test-particle model and trace relativistic electrons at discrete energies between $4.5 \text{ keV} \leq E \leq 100 \text{ MeV}$ while exposed to these fields. For each location with respect to Jupiter's current sheet, electrons of all energies bombard Ganymede's poles with average number and energy fluxes of $1 \cdot 10^8 \text{ cm}^{-2} \text{ s}^{-1}$ and $3 \cdot 10^9 \text{ keV cm}^{-2} \text{ s}^{-1}$, respectively. However, bombardment is locally inhomogeneous: poleward of the open-closed field line boundary, fluxes are enhanced in the trailing hemisphere but reduced in the leading hemisphere. When embedded within the Jovian current sheet, closed field lines of Ganymede's minimagnetosphere shield electrons below 40 MeV from accessing the equator. Above these energies, equatorial fluxes are longitudinally inhomogeneous between the sub-Jovian and anti-Jovian hemispheres, but the averaged number flux ($4 \cdot 10^3 \text{ cm}^{-2} \text{ s}^{-1}$) is comparable to the flux deposited here by each of the dominant energetic ion species near Ganymede. When located outside of the Jovian current sheet, electrons below 100 keV enter Ganymede's minimagnetosphere via the downstream reconnection region and bombard the leading apex, while electrons of all energies are shielded from the trailing apex. Averaged over a full synodic rotation period of Jupiter, the energetic electron flux pattern agrees well with brightness features observed across Ganymede's polar and equatorial surface.

1. Introduction

Ganymede (radius $R_G = 2,634 \text{ km}$) is the largest satellite in the solar system and the only moon known to possess its own intrinsic magnetic field (Kivelson et al., 2002). The magnitude of this permanent field on Ganymede's surface exceeds the local Jovian magnetospheric field by approximately an order of magnitude and is strong enough to stand off the local Jovian field and magnetospheric plasma approximately $2R_G$ upstream of the moon (Kivelson et al., 2004). Hence, a "minimagnetosphere" is formed and Ganymede's equator is surrounded by a region of closed field lines (with both foot points of each field line connected to the moon's surface; e.g., Gurnett et al., 1996; Kivelson et al., 1996). This closed field line region extends to latitudes approximately 40° north and south of the geographic equator, with a slight variation as a function of longitude (Khurana et al., 2007). Poleward of these latitudes, the magnetic field lines are open: one foot point of the field is attached to Ganymede, whereas the other is attached to Jupiter.

Remote observations and modeling of Ganymede's interior suggest that it is fully differentiated. Putative layers include a metal core (e.g., Anderson et al., 1996; Sohl, 2002) as well as a conductive, liquid ocean below an icy outer crust (e.g., Kivelson et al., 2002; Saur et al., 2015; Zhang, 2003). Due to the 9.6° tilt between Jupiter's magnetic and rotational axes, the Jovian magnetospheric field near Ganymede varies in time with a 10.5 hr periodicity that is mainly driven by Jupiter's synodic rotation (Seufert et al., 2011). Thus, while a dynamo within the metallic core sustains Ganymede's primary magnetic field (Kimura et al., 2009; Schubert et al., 1996), currents induced within its subsurface ocean generate a secondary field detectable outside of the moon (Kivelson et al., 2002; Saur et al., 2015).

Besides the primary and secondary magnetic field, the magnetospheric environment near Ganymede is further perturbed by currents that stem from the moon's interaction with the ambient Jovian plasma. Ganymede orbits Jupiter at a distance of $15 R_J$ (radius of Jupiter $R_J = 71,492$ km) and always remains well inside of Jupiter's magnetosphere (Joy et al., 2002). Since the moon's 172 hr orbital period exceeds Jupiter's rotation period, Ganymede represents an obstacle to the azimuthally drifting plasma that nearly corotates with the giant planet (Kivelson et al., 2004). These thermal ions and electrons (with energies $E \leq 10$ keV; e.g., Belcher, 1983) impinge onto Ganymede's orbital trailing (i.e., ramside) hemisphere as they continually overtake the moon at a relative velocity of nearly 140 km s^{-1} . The average mass of these low-energy ions near Ganymede is 14 amu, with ion and electron number densities that fluctuate between 1 and 10 cm^{-3} as Jupiter's magnetospheric plasma sheet sweeps over the moon (Bagenal et al., 2016; Kivelson et al., 2004).

As this plasma encounters Ganymede, Jovian field lines, frozen-in to the corotating thermal plasma, pile up at the moon's trailing (i.e., ramside) hemisphere, drape around the satellite, and generate electromagnetic perturbations near the moon. In this hemisphere, the interaction compresses Ganymede's magnetic field and shifts the separatrices between the open and closed field lines poleward; in the orbital leading (i.e., wakeside) hemisphere, this open-closed field line boundary (OCFB) is pushed equatorward (e.g., Jia et al., 2008, 2009). Further contributions to the plasma interaction currents stem from the deflection of the thermal Jovian plasma by Ganymede's dilute exosphere (e.g., Hall et al., 1998; Paty & Winglee, 2006). Local acceleration of the thermal plasma in these electromagnetic fields creates the moon's ultraviolet aurora (Eviatar et al., 2001; Feldman et al., 2000; McGrath et al., 2013). Since the ambient plasma near Ganymede is sub-Alfvénic and submagnetosonic (Kivelson et al., 2004), currents generated locally by this plasma interaction close at large distances to the moon by currents that flow along the characteristics of the moon's Alfvén wings. These nonlinear standing Alfvén waves connect Ganymede to Jupiter's polar ionosphere (Neubauer, 1998), leaving a footprint signature in the ultraviolet Jovian aurora (e.g., Clarke et al., 2002; Szalay et al., 2020).

In addition to the low-energy thermal population, the Jovian magnetospheric plasma near Ganymede consists of ions and electrons with energies $E \geq 10$ keV that likely extend up to approximately 100 MeV (e.g., Divine & Garrett, 1983). These energetic particles bounce between Jupiter's magnetic poles as they drift azimuthally through the magnetosphere. Near Ganymede, the number densities of these energetic ions and electrons are orders of magnitude smaller than those of the thermal particle population (e.g., Cooper et al., 2001; Mauk et al., 2004). Since the energetic *electrons* contribute to less than 5% of the total plasma pressure near Ganymede's orbit (compared to a nearly 90% contribution to the total pressure from energetic *ions* alone; see Kivelson et al., 2004), their behavior can be well represented as *test particles* exposed to a predefined electromagnetic field configuration.

Despite their low densities in the ambient plasma, the energetic particle population drastically alters Ganymede's markedly inhomogeneous surface (Cooper et al., 2001). The moon's visibly dark equatorial region with ram/wake asymmetries in brightness patterns as well as in the surface concentrations of O_2 (Calvin & Spencer, 1997; Spencer et al., 1995) and O_3 (Noll et al., 1996) have been suggested to be the result of energetic charged particle bombardment. At higher latitudes, bright surface features in part generated by precipitation of thermal and energetic ions characterize the moon's surface (e.g., Fatemi et al., 2016; Khurana et al., 2007; Smith et al., 1979). In addition, particle precipitation onto these regions helps sustain Ganymede's tenuous exosphere via sputtering of its surface ices (e.g., Carnielli et al., 2020; Ip et al., 1997; Paranicas et al., 1999; Plainaki et al., 2015; Poppe et al., 2018). The energetic particles may also partially ionize the resulting neutral exosphere, although to a much lesser degree than the thermal plasma at lower energies (see, e.g., Carnielli et al., 2019; Erdman & Zipf, 1986; Saur et al., 1998; Wells et al., 1971).

Irradiation of Ganymede by energetic particles also affects the ice state and composition of the surface, as well as its thermal properties. Surface ice states on outer solar system bodies can be described as either crystalline or amorphous. The balance between these two states likely depends on the competing processes of thermal annealing (which transforms amorphous ice into crystalline ice) and particle irradiation (which destroys the regular, repeating lattice structure of crystalline ice to produce amorphous ice). At Ganymede, Galileo observations revealed a heterogeneous mix of both amorphous and crystalline ice distributed across the moon's surface. Hansen and McCord (2004) have shown that low-latitude ice in the anti-Jovian hemisphere is mainly crystalline, while ice in the trailing hemisphere is more amorphous. Similarly, these authors found that the ice is predominantly amorphous at high latitudes as well.

These observations have been correlated with energetic ion bombardment of Ganymede (e.g., Cooper et al., 2001; Khurana et al., 2007), and modeling studies have demonstrated enhanced precipitation not only onto the moon's poles (Fatemi et al., 2016) but also onto the low-latitude, trailing hemisphere (Poppe et al., 2018). While many studies of the irradiation of Ganymede's surface have focused on the role of energetic ions, it has been shown that electrons also alter the crystalline structure of ice (Baragiola, 2003). At temperatures below 70 K (i.e., near Ganymede's poles; see Squyres, 1980), Dubochet and Lepault (1984) and Loeffler et al. (2020) have shown that energetic electrons effectively amorphize ice.

Radiolysis of the ice generated by energetic particle irradiation also drives the production of various chemical compounds (such as hydroxide, hydrogen peroxide, as well as other trace species; e.g., Johnson & Quickenden, 1997; Teolis et al., 2017). In addition to ion radiolysis, multiple laboratory studies have demonstrated the importance of energetic electrons (with energies near 10 keV) in the radiolytic production of compounds within ices across a wide range of temperatures (from 10 to 120 K), the upper end of which are relevant for Ganymede's surface (for more details, see, e.g., Hand & Carlson, 2011; Mahjoub et al., 2016; Zheng et al., 2006). Hence, the contribution of energetic ions alone is *not* sufficient to explain the observed distribution of chemical species across Ganymede's surface; energetic electron bombardment needs to be taken into account as well. Indeed, previous studies of Europa have documented the importance of electron precipitation in the correlation between irradiation patterns and the surface distribution of various species (see, e.g., Paranicas et al., 2001; Dalton et al., 2013; Nordheim et al., 2018).

Finally, the thermal properties of ices are altered by energetic electron irradiation. Thermal inertia anomalies across the surfaces of Saturn's moons Mimas and Tethys have been observed by the Cassini spacecraft (i.e., the so-called "PacMan" features; e.g., Howett et al., 2011, 2012, 2020) and have been correlated with regions of enhanced energetic electron bombardment (Nordheim et al., 2017; Paranicas et al., 2014). Schaible et al. (2017) have explained these features using a model of ice grain sintering for these Saturnian moons, whereby individual ice molecules, liberated by electron irradiation of the surface, accumulate between the contact points of ice grains, thereby increasing their overall contact area. In turn, the effective thermal inertia of the surface ice is increased, yielding the remotely observed thermal inertia and temperature anomalies. However, the electromagnetic environments of these Saturnian moons are vastly different from that of Ganymede, and one would not expect an identical lens-like thermal inertial anomaly to form a priori. Regardless, sintering of surface grains by irradiation of energetic electrons may nevertheless be an active process in shaping the thermal properties of Ganymede's surface ice.

Thus, our ability to understand the complex processes that contribute to the generation of disparate features across Ganymede's surface is directly dependent on constraining the dynamics, intensity, and distribution of the charged particles as they bombard the moon's surface. However, spatially resolved patterns of energetic *electron* precipitation onto the surface remain unconstrained.

2. Previous Studies on Energetic Particle Bombardment of Ganymede

Ganymede's interaction with the thermal Jovian magnetospheric plasma drastically affects the moon's plasma environment. Magnetospheric field lines pile up and drape around the moon (e.g., Paty & Winglee, 2004, 2006), compressing the minimagnetosphere and resulting in strong magnetopause and tail currents that close nearly 50% of the Alfvén wing current and further perturb the electromagnetic fields (Jia et al., 2008). Deflection of the ambient plasma flow around Ganymede generates additional perturbations in the electric field near the moon (see, e.g., the models presented in Fatemi et al., 2016; Poppe et al., 2018).

However, as a first approximation to constrain energetic ion fluxes onto Ganymede's surface, Cooper et al. (2001) represented the local electromagnetic environment within $2 R_G$ of the moon using a superposition of a permanent dipole field centered at Ganymede with the local Jovian magnetospheric background field alone (i.e., without including plasma interaction effects). In addition, these authors did not consider the influence of an electric field (neither a convective electric field nor the electric field perturbations resulting from Ganymede's interaction with the thermal plasma) on energetic particle bombardment. Using these approximations, Cooper et al. (2001) found that the energetic proton precipitation pattern is nonuniform with latitude and longitude on the surface: protons with energies $E \leq 5$ MeV are shielded from the trailing, equatorial surface but are able to precipitate along the open magnetic field lines at higher latitudes (see Figure 10 in that work).

For energetic electron irradiation of Ganymede, these authors used a method introduced by Størmer (1955) to analytically estimate, as a function of energy, the ability of Ganymede's dipolar field to shield electrons from reaching the surface. Cooper et al. (2001) estimated that electrons with energies $E \leq 100$ MeV cannot penetrate through the closed field line region and are thus unable to precipitate onto the equator. However, at latitudes poleward of the OCFB (i.e., along open field lines of the dipolar field), their findings suggest that electrons at all energies have uniform access to Ganymede's surface.

Using these methods, Cooper et al. (2001) estimated the number and energy fluxes of ions and electrons onto Ganymede's surface during the Galileo G2 flyby. Since their findings suggest that electrons with energies below 100 MeV are unable to precipitate onto equatorial latitudes, these authors do not provide any constraints for electron fluxes in this region. However, Cooper et al. (2001) estimate that electrons at energies $20 \text{ keV} \leq E \leq 40 \text{ MeV}$ are responsible for a number flux of $3.1 \cdot 10^7 \text{ cm}^{-2} \text{ s}^{-1}$ into Ganymede's poles, with an associated energy flux of $3.4 \cdot 10^9 \text{ keV cm}^{-2} \text{ s}^{-1}$. These values are nearly 4 and 2 times larger, respectively, than the polar fluxes of ions at energies $E \leq 100$ MeV. Cooper et al. (2001) therefore conclude that while *ions* are responsible for the majority of energy deposited onto Ganymede's equator, *electrons* are the dominant carriers of energy onto the poles. A similar conclusion was reached by Paranicas et al. (1999), who determined that precipitating energetic electrons substantially modify the ice at polar latitudes. These authors also suggested that the energetic electron population likely does *not* substantially contribute to generation of aurora or airglow at Ganymede (see also Eviatar et al., 2001; McGrath et al., 2013).

For electrons at even lower energies ($E \leq 4.5$ keV), Frank et al. (1997) used data from the Galileo *Plasma Subsystem* (PLS) obtained during the G2 encounter to estimate the electron flux onto the Ganymede's poles. Similar to Cooper et al. (2001), these authors assumed electron bombardment within the high-latitude open field line region to be homogeneous. Frank et al. (1997) calculated a polar energy flux on the order of $6 \cdot 10^8 \text{ keV cm}^{-2} \text{ s}^{-1}$, while Delitsky and Lane (1998) used this value to derive a corresponding polar number flux of $2 \cdot 10^8 \text{ cm}^{-2} \text{ s}^{-1}$. Thus, while the number flux of electrons into Ganymede's poles may be dominated by low-energy ($E \leq 4.5$ keV) electrons, the energy flux is dominated by electrons at energies above 20 keV (see also discussion in Cooper et al., 2001).

However, none of these previous studies have considered the influence of Ganymede's interaction with the thermal Jovian magnetospheric plasma on energetic particle fluxes. As an improvement to these simplifying assumptions, Plainaki et al. (2015) used output from an MHD simulation (Jia et al., 2009) to consider the effect of moon's interaction with the thermal Jovian magnetospheric plasma in shaping the electromagnetic field environment. These authors studied precipitation of energetic (10 keV) O^+ ions onto the moon and found that the differential surface flux is not uniform but rather enhanced along (and poleward of) the OCFB. Plainaki et al. (2015) demonstrated the importance of including currents driven by Ganymede's thermal plasma interaction in order to accurately describe the dynamics of (and the surface erosion by) energetic ions that generate the moon's exospheric environment. Fatemi et al. (2016) used a hybrid (kinetic ions and fluid electrons) simulation to model the interaction between Ganymede's induced and intrinsic magnetic field with the upstream magnetospheric plasma. These authors presented a map displaying the surface number flux of ions with energies from $1 \text{ keV} \leq E \leq 10 \text{ MeV}$ during the G8 flyby and found that the number flux onto Ganymede's poles locally exceeds the flux onto the trailing equatorial surface by up to 3 orders of magnitude. In addition, this study provided further evidence of a dependence of the observed high-latitude brightness features on energetic ion precipitation. The interaction between Ganymede's magnetic field and the impinging thermal Jovian plasma compresses the minimagnetosphere, shifting the surface location of the OCFB, resulting in a correlation between the open field line region and energetic ion bombardment (see also Khurana et al., 2007). Using the same electromagnetic field output from the G8 hybrid simulation of Fatemi et al. (2016), Poppe et al. (2018) investigated the dynamics and precipitation patterns of energetic H^+ , O^{2+} , and S^{3+} ions at energies between 1 keV and 10 MeV onto Ganymede. Poppe et al. (2018) found that the total high-latitude (poleward of 60°) number flux exceeds the flux onto the equatorial *leading* hemisphere by more than an order of magnitude, while the polar flux exceeds the flux onto the equatorial *trailing* hemisphere by a factor of over 200.

Each of these previous studies (Fatemi et al., 2016; Plainaki et al., 2015; Poppe et al., 2018) has investigated the influence of Ganymede's perturbed electromagnetic environment on energetic ion precipitation when the moon is located near the center of Jupiter's magnetospheric current sheet; any variability in these patterns as a function of System III longitude remains unconstrained. However, over a full synodic rotation,

the magnitude of the Jovian field near Ganymede's orbit changes by a factor of approximately 2 (e.g., Jia et al., 2008; Kivelson et al., 2004). In addition, when Ganymede is located near the center of Jupiter's current sheet, the orientation of the magnetospheric field is mainly southward with only a slight nonzero component (below approximately 15 nT) that is either parallel or antiparallel to the direction of corotation due to corotation lag (e.g., Hill, 1979). Far above or below the center, however, the field has a strong component directed either away or toward Jupiter, respectively. Besides these changes in the magnetospheric field, the ambient number densities of the thermal ion and electron populations near the moon vary by up to an order of magnitude (Bagenal & Delamere, 2011; Kivelson et al., 2004). Hence, the ambient electromagnetic field configuration, Ganymede's induced field, and the moon's interaction with the magnetospheric plasma all change as a function of System III longitude resulting in a variable, inhomogeneous electromagnetic environment (see, e.g., Dorelli et al., 2015; Fatemi et al., 2016; Jia et al., 2008; Tóth et al., 2016; Wang et al., 2018). Indeed, the variability in Ganymede's plasma environment over a synodic rotation was observed during the six Galileo encounters of the moon, as discussed in detail by multiple studies (e.g., Duling et al., 2014; Jia et al., 2009; Kivelson et al., 2002; Paty & Winglee, 2004, 2006; Zhou et al., 2019).

To calculate the energetic *ion* flux onto Ganymede's surface, previous studies have included particles with energies extending to 100 MeV (e.g., Cooper et al., 2001). For *electrons*, however, studies have investigated the flux onto Ganymede's poles only for energies $E \leq 4.5$ keV (e.g., Frank et al., 1997) or at higher energies between $20 \text{ keV} \leq E \leq 40 \text{ MeV}$ (Cooper et al., 2001). The contribution of the electron population at energies between $4.5 \text{ keV} \leq E \leq 20 \text{ keV}$ and from $40 \text{ MeV} \leq E \leq 100 \text{ MeV}$ to the number and energy flux onto Ganymede's surface are unknown. In addition, the fluxes of high-energy electrons into Ganymede's equator remain unconstrained.

Yet electrons with energies between $4.5 \text{ keV} \leq E \leq 20 \text{ keV}$ and extending up to $E = 100 \text{ MeV}$ are prominent throughout the Jovian magnetosphere (de Pater & Dunn, 2003; de Soria-Santacruz et al., 2016; Garrett et al., 2012; Kollmann et al., 2018). At Europa, 100 MeV electrons may indeed play an important role in the energy deposition into the moon's surface (Paranicas et al., 2001; Truscott et al., 2011). High-energy magnetospheric electrons also contribute to the destruction of any potential biosignatures from Europa's subsurface ocean that may be located beneath the icy crust (Johnson et al., 2004; Nordheim et al., 2018), as they deposit their energy at much greater depths than are possible by energetic ions alone (Hand & Carlson, 2011). Moreover, despite their dominant contribution to the total particle flux of Ganymede's polar surface (Cooper et al., 2001), no study has investigated the spatial distribution of the electron surface fluxes. In addition, the effect of Ganymede's interaction with the thermal Jovian magnetospheric plasma on energetic electron dynamics—and any variability thereof—remains unconstrained. Nevertheless, multiple studies have documented the importance of including the locally perturbed plasma environment in order to capture and accurately model spatial inhomogeneities in the precipitation of energetic ions at Ganymede (Fatemi et al., 2016; Plainaki et al., 2015; Poppe et al., 2018). Similarly, recent studies have shown the necessity of including the perturbed plasma environments of Callisto and Europa (whose interactions with the ambient plasma play an even stronger role in shaping their electromagnetic environments) to understand energetic electron and ion bombardment of these moons (Breer et al., 2019; Liuzzo et al., 2019a, 2019b).

As these high-energy electrons can affect the physical and chemical state of Ganymede's icy surface, it is therefore worthwhile to perform a more complete treatment of their dynamics near the moon and to investigate the resulting precipitation and flux deposition onto Ganymede's regolith. For these reasons, this study will consider the moon's perturbed electromagnetic environment for multiple locations in the Jovian magnetosphere while investigating the surface bombardment patterns and fluxes of energetic electrons between $4.5 \text{ keV} \leq E \leq 100 \text{ MeV}$. This study is structured as follows: Section 3 describes the hybrid model used to constrain Ganymede's thermal magnetospheric plasma environment and provides a brief overview of the local electromagnetic perturbations present during the three Galileo flybys on which this study focuses. Section 4 includes a discussion of Ganymede's ambient energetic electron environment and introduces the test-particle approach we use to model electron dynamics near the moon. Results of these particle tracing simulations—including spatially resolved maps of the energetic electron number and energy flux onto Ganymede's surface over large timescales—are presented in section 5. Finally, section 6 includes a brief discussion on the remaining open questions regarding energetic electron dynamics near Ganymede, and conclusions are presented in section 7.

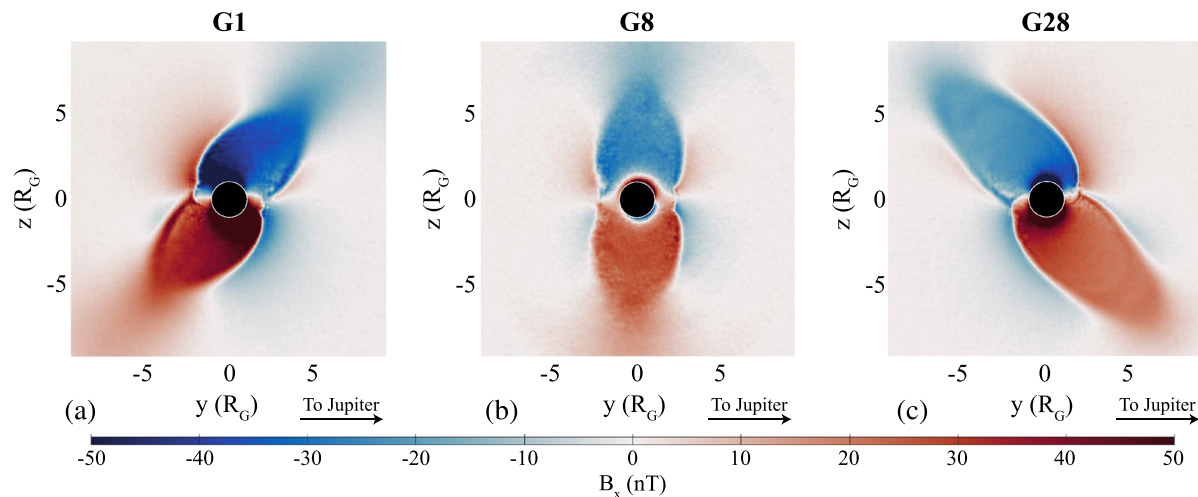


Figure 1. B_x component of the magnetic field near Ganymede during the Galileo (a) G1, (b) G8, and (c) G28 encounters in the $x = 0$ plane, as viewed from a point downstream of the moon. The intersection of Ganymede's surface with this plane is denoted by the white circle. The ambient $B_{x,0}$ component during each of these flybys was $B_{x,0} = 0$ nT, so (red hues) $B_x > 0$ denotes perturbations above the background component, whereas (blue hues) $B_x < 0$ denotes a decrease. The GphiO coordinate system in used (see text).

3. Modeling Ganymede's Thermal Plasma Environment: The Galileo G1, G8, and G28 Flybys

To study the effect that Ganymede's perturbed electromagnetic environment has on energetic electron bombardment patterns and surface fluxes, as well as any variability thereof, this study will use output from the hybrid simulations of Fatemi et al. (2019b). These authors investigated features of Ganymede's perturbed electromagnetic environment by including contributions from the moon's permanent and induced magnetic field as well as currents generated by the interaction with the thermal Jovian plasma for each of the six Galileo flybys of the moon. Further details (beyond what is provided below) can be found in Fatemi et al. (2016) or Poppe et al. (2018).

In order to obtain a representative sample of the variability in the ambient magnetospheric environment around Ganymede during a synodic rotation, we consider the moon's location during three Galileo flybys: G1, G8, and G28. Each of these encounters occurred with Ganymede located at a different distance to the center of Jupiter's magnetospheric current sheet. By focusing on these three flybys, we are able to correlate any changes in the energetic electron fluxes onto the surface with differences in Ganymede's thermal plasma interaction as a function of distance to the Jovian current sheet (i.e., with System III longitude). During G1, Ganymede was located approximately $2.5 R_J$ above the center of Jupiter's magnetospheric current sheet, near a System III longitude of $\lambda_{III} \approx 175^\circ$ and at a Jovian magnetic latitude of approximately 8.6° . Alternatively, the G28 encounter occurred when Ganymede was nearly $2.5 R_J$ below the center of the Jovian current sheet at a magnetic latitude of approximately -8.2° , near a System III longitude of $\lambda_{III} \approx 350^\circ$. In contrast to these flybys at large Jovian magnetic latitudes, G8 occurred when Ganymede was embedded within the center of Jupiter's magnetospheric current sheet at a magnetic latitude of only 0.13° , near $\lambda_{III} \approx 290^\circ$.

Figure 1 displays the B_x component of the magnetic field near Ganymede for the G1, G8, and G28 flybys in the $x = 0$ plane as viewed from downstream of the moon, as obtained from the hybrid model output of Fatemi et al. (2016). This figure uses the Ganymede-centered, Cartesian, GphiO coordinate system: unit vector \hat{x} is aligned with the azimuthal corotation direction (out of the page in the figure), \hat{y} points toward Jupiter (to the right), and \hat{z} is aligned with the Jovian spin axis (upward in the figure), completing the right-handed system. Signatures of field line draping and Ganymede's northern and southern Alfvén wings are clearly discernible in each panel, with $B_x < 0$ in the moon's northern hemisphere and $B_x > 0$ in the southern hemisphere during each flyby. At the time of the G1 encounter (Figure 1a), the magnetospheric background field was $\mathbf{B}_0 = [0\hat{x} - 79\hat{y} - 79\hat{z}]$ nT. This orientation resulted in a 45° inclination of the Alfvén wing characteristics against the $y = 0$ plane, with the northern wing tilted into the *sub*-Jovian ($y > 0$) hemisphere and the southern wing tilted toward the *anti*-Jovian ($y < 0$) hemisphere. Alternatively for G28 (Figure 1c), the

background field was nearly mirrored against the $y = 0$ plane compared to the field during G1, with $\mathbf{B}_0 = [0\hat{x} + 77\hat{y} - 76\hat{z}]$ nT. Hence, during this flyby, Ganymede's two Alfvén wings were in opposite hemispheres compared to G1. During G8 however (Figure 1b), since the background field was almost entirely along the $-z$ direction with $\mathbf{B}_0 = [0\hat{x} - 6\hat{y} - 77\hat{z}]$ nT, the two Alfvén wings were nearly symmetric with respect to the $y = 0$ plane (tilted at an angle of just 4°). In addition to the changes in the ambient magnetic field during G1, G8, and G28, the orientation and magnitude of Ganymede's magnetic moment (resulting from its permanent *and* induced dipole) were different during each of these three encounters (see, e.g., Table 2 of Jia et al., 2008).

Any numerical simulation of Ganymede's interaction with the thermal Jovian plasma can only calculate the electromagnetic field perturbations within a finite volume close to the moon. For the hybrid simulations used in this study, these perturbations are constrained within a box extending approximately $10 R_G$ from the center of Ganymede in each direction. Beyond these distances, any plasma interaction effects outside of the highly localized Alfvén wings have entirely faded away (see, e.g., Figure 1 in this study or Fatemi et al., 2016; Poppe et al., 2018). Properties of the upstream plasma required as input for the hybrid simulation of each flyby are documented in detail by Fatemi et al. (2016).

4. Modeling Energetic Electrons Near Ganymede

In the magnetospheric field near the orbit of Ganymede, the gyroradius r_g of a relativistic 15 MeV electron (with Lorentz factor $\gamma \approx 30.5$) is $r_g \approx 0.25 R_G$. Electrons with energies above approximately 60 MeV have gyroradii that approach the radius of the moon. Hence, for the range of energies considered in this study ($4.5 \text{ keV} \leq E \leq 100 \text{ MeV}$), electron dynamics *cannot* be described using a fluid or guiding center approach: the gyration of each individual electron may generate asymmetries in the bombardment patterns and must be taken into account. Since the hybrid approach used to model Ganymede's interaction with the thermal plasma treats electrons as a single massless, charge-neutralizing fluid, it is not possible to self-consistently include a high-energy electron population into that model. For this reason, we import the electromagnetic fields calculated by the hybrid model into the Galilean *Energetics Tracing Model* (GENTOO; Liuzzo et al., 2019b) to study energetic electrons near Ganymede. Similar techniques of combining output of a hybrid model with a test particle simulation have been used to study energetic ion and electron dynamics at various Jovian moons including Ganymede (Fatemi et al., 2016; Poppe et al., 2018), Callisto (Liuzzo et al., 2018, 2019a, 2019b), and Europa (Arnold et al., 2019, 2020; Breer et al., 2019), as well as multiple moons of Saturn (e.g., Feyerabend et al., 2015; Kotova et al., 2015; Krupp et al., 2020; Regoli et al., 2016).

An exhaustive discussion on the numerics of the electron version of GENTOO used in this study has been presented in section 2 of Liuzzo et al. (2019a), so only a brief review is provided here. GENTOO solves the Lorentz force equation for relativistic electrons embedded in an electromagnetic field using the second-order numerical solver presented in Vay (2008). To prevent simulating particles that would potentially neither interact with Ganymede's local electromagnetic environment nor precipitate onto the moon, GENTOO uses a negative time step: electrons are initialized on Ganymede's surface at a given energy and direction and are traced *backward* in time. For this study, we initialize electrons at 26 individual energies between $4.5 \text{ keV} \leq E \leq 100 \text{ MeV}$, discretized such that the change in an electron's Lorentz factor γ between any two consecutive energies is linear. Each of the 26 GENTOO simulations at a single energy uses a spatial resolution of 2° in latitude and 4° in longitude to discretize Ganymede's surface, with an angular velocity resolution of 2° in zenith and 4° in azimuth. Hence, at each of the 8,100 surface points, we define a "sphere" in velocity space at which 8,100 electrons are initialized, with a radius defined by the given energy. Note that at every surface point, *exactly half* of the 8,100 electron trajectories are "shadowed" by the presence of Ganymede and are immediately removed from the simulation. Thus, for each of the 26 discrete energies, the trajectories of nearly 33 million individual electrons are computed, assuring sufficiently high resolution in position and velocity space.

One of two outcomes occurs for each electron *backtraced* during a GENTOO simulation. The first is that, at any point during its tracing, the electron's trajectory \mathbf{r} intersects Ganymede's surface; that is, $|\mathbf{r}| \leq R_G$. Such an electron is "forbidden" and cannot contribute to the flux onto the point at which it was initialized: in order to reach this location in a forward-tracing approach, the electron would need to travel *through* the solid body of Ganymede. The second outcome for a backtraced electron is that it *never* again intersects Ganymede's

surface after initialization. Such an electron is “allowed”; in a forward-tracing approach, it would precipitate onto the moon and contribute to the energetic electron flux onto that point.

However, a more sophisticated boundary condition is required to determine when an electron is “allowed”: simply exiting the domain of the hybrid simulation is not enough to ensure the electron’s trajectory will not intersect Ganymede’s surface due to the rapid bounce times of energetic electrons through Jupiter’s magnetosphere. Consider the following example: the time required for a 500 keV electron to leave Ganymede’s local environment, travel through Jupiter’s magnetosphere to large Jovian magnetic latitudes where it mirrors, and then return to the moon is on the order of 10 s (Williams & Mauk, 1997). In this time frame, assuming an undisturbed flow of the upstream plasma at approximately 80% of the local corotation velocity relative to Ganymede’s orbital velocity, a magnetospheric field line would only travel on the order of $0.5 R_G$ along the direction of corotation; mass loading would reduce this distance even further. Hence, energetic electrons trapped on this field line may potentially reencounter the moon after initially leaving its local magnetospheric environment and impact on a subsequent bounce, thereby becoming “forbidden.” Therefore, in order to consider this bounce motion, we combine the local hybrid model of Ganymede’s perturbed electromagnetic environment with a global model of Jupiter’s magnetospheric field. Contributions to the field from internal and external sources are included by applying a combination of the VIP4 (Connerney et al., 1998) and the Khurana (1997) magnetosphere models. For further details on the coupling of these models, see Seufert et al. (2011) or Figure 3 of Liuzzo et al. (2019a).

We note that electromagnetic waves resonant with energetic electrons have been detected throughout the magnetospheres of Jupiter and Saturn (e.g., Menietti et al., 2012), with indications of enhanced electromagnetic activity in the vicinity of icy moons (Shprits et al., 2018). Within approximately $8 R_G$ of Ganymede, the Galileo Plasma Wave Science experiment detected a variety of intense electromagnetic waves (Gurnett et al., 1996), including strong whistler mode chorus waves (Shprits et al., 2018). While these waves may accelerate energetic electrons and scatter their pitch angles via gyroresonant interactions, the degree to which this process affects electron dynamics remains unknown. However, Williams and Mauk (1997) and Tripathi et al. (2014) suggest that such wave-particle interactions do *not* significantly scatter the pitch angle of energetic electrons over a few bounce periods (i.e., the timescales upon which this study focuses). We therefore assume that wave-particle interactions near Ganymede are of secondary importance for understanding the dynamics and bombardment patterns of energetic electrons onto the moon, and they are not considered here. Moreover, the currently limited data set of electromagnetic wave observations—not only near Ganymede but entirely along the Jovian magnetospheric field lines connected to the moon—precludes quantitative modeling of these effects, an exercise that is thus reserved for a future study.

During its bounce motion, an electron is displaced azimuthally in Ganymede’s orbital plane by an amount determined by the combination of its corotational and gradient-curvature drifts. Using Equations 5–9 of Liuzzo et al. (2019a), we calculate this azimuthal displacement r_{eq} of an electron during its half bounce period based on its energy and pitch angle as it leaves the domain of the hybrid simulation (see Figure 2). Note that the electron loss cone associated with Jupiter’s atmosphere is below 1° near Ganymede’s orbital position (i.e., well below the angular resolution of the model), and the number of electrons lost before mirroring is negligible (see, e.g., Williams et al., 1997, 1998). After returning, the electron is reinjected into the same face of the hybrid simulation domain from which it exited. However, the electron’s x position is displaced by the *negative* value of the calculated azimuthal displacement during its half bounce (in the *backtracing* technique), with the component of its velocity that is parallel to the magnetic field reversed. Note that the *gyrophase* at which an electron is reinserted into the simulation domain after bouncing has no relevance as to whether or not it will become forbidden: in order for an electron to gyrate around Ganymede and avoid intersecting the moon, its gyroradius must be $r_g \approx R_G$. Yet the azimuthal displacement of an electron with an energy at which this condition is satisfied (i.e., $E \approx 60$ MeV) exceeds the size of the hybrid simulation domain (see Figure 2 as well as the discussion provided in Liuzzo et al., 2019a).

After a *backtraced* electron is reinserted into the simulation domain, it again travels through the perturbed electromagnetic fields near Ganymede until either impacting the moon (where it becomes forbidden) or exiting the hybrid simulation domain. In the latter case, the electron’s azimuthal displacement r_{eq} during a half bounce is again calculated and the electron is reinjected into the simulation domain. For any given electron, this procedure may repeat multiple times before its bounce motion carries it beyond the upstream ($-x$) or downstream ($+x$) face of the hybrid simulation, when it is finally considered “allowed.” At these

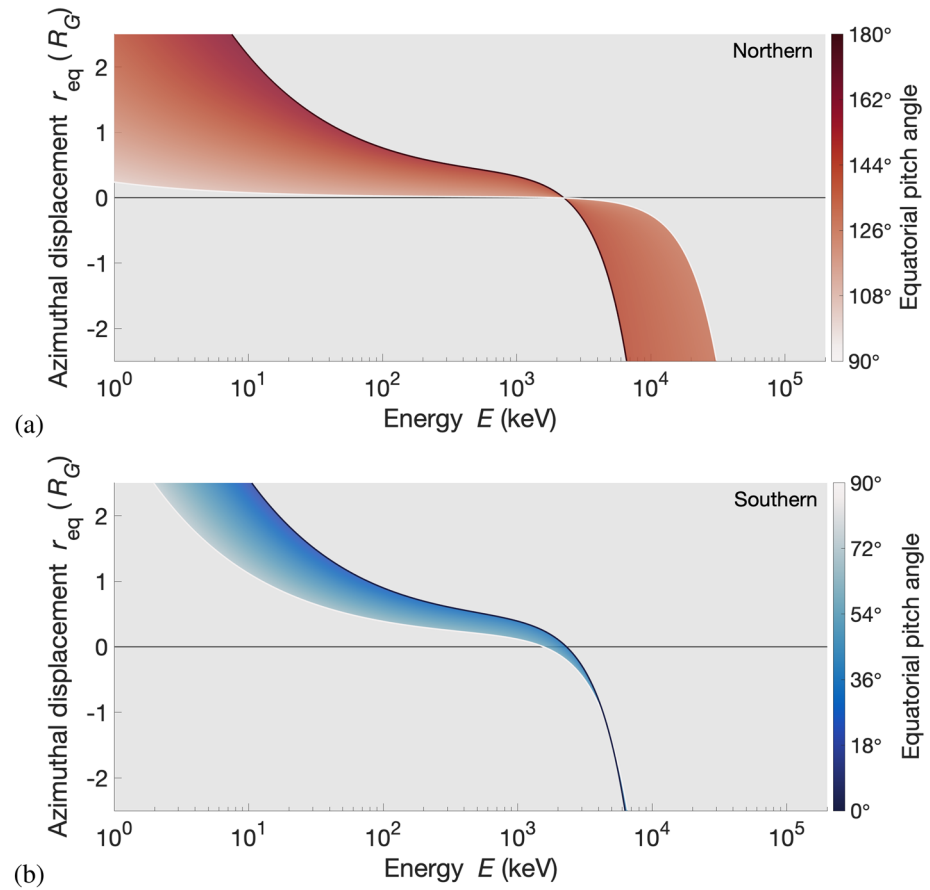


Figure 2. Azimuthal displacements r_{eq} of electrons mirroring at (a) northern and (b) southern magnetic latitudes of Jupiter as a function of energy E_0 and equatorial pitch angle in the ambient plasma near Ganymede. The values correspond to Ganymede’s location within the Jovian magnetosphere during the G8 flyby of Galileo (i.e., near the center of Jupiter’s magnetospheric current sheet). Curves that bound the shaded regions in each panel are included, displaying the azimuthal displacements for electrons at four select pitch angles: (panel a, red) 180° , (panel a, white) 91° , (panel b, white) 89° , and (panel b, blue) 0° . The ambient magnetospheric field near Ganymede has a strong $-\hat{z}$ component, so electrons with a pitch angle of 0° initially travel southward before mirroring and returning to the moon, while electrons with a 180° pitch angle initially travel northward. The gray horizontal line in each panel denotes an azimuthal displacement of $r_{\text{eq}} = 0 R_G$. Note that the opening angle of the loss cone near Ganymede’s orbit associated with Jupiter’s atmosphere is below 1° and that electrons with a pitch angle of exactly 90° do not exhibit any bounce motion.

azimuthal distances of $|x| \gtrsim 10 R_G$ from the moon, the ambient electromagnetic fields are homogeneous (see section 3), and it would not be possible for an electron to impact Ganymede on any successive bounce as the particle continues to travel to subsequently larger azimuthal distances.

Due to its charge dependence, the gradient-curvature drift velocity of an electron points in the direction opposite to corotation (e.g., Khurana et al., 2008; Krupp et al., 2013; Liuzzo et al., 2019a). Hence, at a certain “critical” energy E_c , this drift velocity exactly cancels the corotational drift velocity, and a bouncing electron is *not* azimuthally displaced with respect to the moon. Close to Ganymede’s orbital position, this “resonance” occurs for electrons with critical energies near $E_c \approx 2 \text{ MeV}$; however, note that the exact value is a function of the magnetic field magnitude as well as the electron’s pitch angle (e.g., Roederer, 1967; Thomsen & Van Allen, 1980). Below the critical energy, electrons are convected toward downstream during their bounce motion (i.e., along the direction of corotation in the moon’s reference frame), while above this energy, they travel toward upstream (i.e., in the anticorotation direction). Note that backtraced electrons with energies E_0 in the ambient plasma near Ganymede that are *below* the critical energy (i.e., with $E_0 < E_c$) are displaced toward *upstream* after bouncing, while backtraced electrons *above* the critical energy ($E_0 > E_c$) are displaced toward *downstream*.

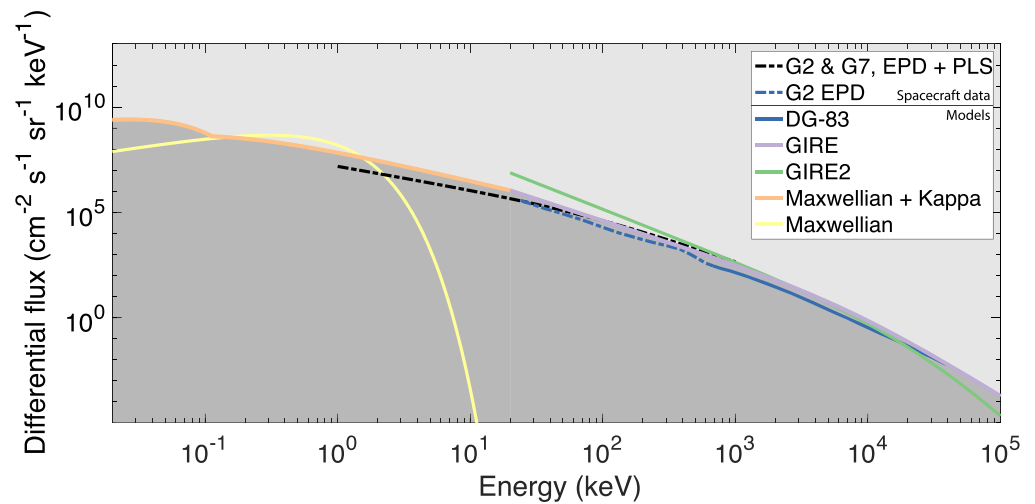


Figure 3. Differential electron number fluxes $J_0(E_0)$ in the ambient, undisturbed plasma near Ganymede. The dashed lines correspond to measurements during the (black) G2 and G7 Galileo flybys from EPD and PLS as presented in Paranicas et al. (1999) or during the (blue) G2 flyby from EPD as presented in Cooper et al. (2001). Solid lines correspond to various models of the differential electron flux. Using (blue) the model of Divine and Garrett (1983), Cooper et al. (2001) extended the EPD measurements during G2 up to energies of 40 MeV. The average fluxes near Ganymede's orbit as estimated by the (purple) GIRE and (green) GIRE2 models are included, as presented in Garrett et al. (2003) and de Soria-Santacruz et al. (2016), respectively. An additional fit (orange) combining a Maxwellian and kappa distribution is included, as presented by Jun et al. (2019). To compare these ambient energetic electron fluxes with the thermal electron population, a (yellow) Maxwellian distribution of the ambient plasma near Ganymede is shown using average values from Kivelson et al. (2004). Shading corresponds to the model curves used to obtain $J_0(E_0)$ for this study.

Figure 2 displays the azimuthal displacement r_{eq} of electrons as a function of energy for Ganymede's position in the Jovian magnetosphere during the G8 flyby (i.e., in Jupiter's postdawn sector located slightly above the center of the magnetospheric current sheet, near $\lambda_{III} \approx 290^\circ$ with a magnetic latitude of $+0.13^\circ$). Figure 2a displays azimuthal displacements for electrons with equatorial pitch angles between 90° and 180° that mirror at northern Jovian magnetic latitudes, whereas Figure 2b shows displacements for electrons with pitch angles of $0-90^\circ$ that mirror at southern magnetic latitudes. Note that the value of a given electron's azimuthal displacement will differ when Ganymede is located at a different position in Jupiter's magnetosphere (e.g., during the G1 or G28 encounters).

Figure 2 illustrates that the exact value of an electron's azimuthal displacement after mirroring r_{eq} is a function of the particle's energy and pitch angle. For an electron at a given energy E_0 in the ambient magnetospheric plasma near Ganymede, this figure also highlights an asymmetry in the azimuthal displacement during G8 between electrons mirroring at northern and southern Jovian latitudes. Since Ganymede was slightly above the center of Jupiter's magnetospheric current sheet, the range of energies where $|r_{eq}| \leq 0.01 R_G$ for northern-mirroring electrons (between approximately $1.1 \text{ MeV} \leq E_0 \leq 2.6 \text{ MeV}$; Figure 2a) is broader than for those that mirror in the south ($1.5 \text{ MeV} \leq E_0 \leq 2.3 \text{ MeV}$; Figure 2b). When above the center of Jupiter's magnetospheric current sheet, the field lines that connect Ganymede to the giant planet's north polar ionosphere are shorter than those that connect in the south. Hence, electrons mirroring at northern Jovian magnetic latitudes return, on average, much closer to Ganymede over a larger energy range after bouncing than their counterparts in the southern hemisphere. The same effect is visible in the bounce motion of electrons near Callisto to a much stronger degree, generating pronounced asymmetries in the energetic electron precipitation patterns onto that moon; see, e.g., Figures 2 and 4 of Liuzzo et al. (2019a).

After energetic electrons have escaped with allowed trajectories, we can determine their contribution to the flux onto Ganymede's surface. In order to do so, we require an expression for the differential electron flux J_0 as a function of energy E_0 measured in the undisturbed plasma near the moon. Figure 3 displays multiple curves of the differential number flux for thermal and energetic electron populations for a wide range of energies ($20 \text{ eV} \leq E_0 \leq 100 \text{ MeV}$), over which the energetic electron fluxes change by more than 13 orders of magnitude. The dashed lines in Figure 3 represent data obtained during two separate Galileo flybys of

Ganymede, whereas solid lines show differential fluxes from various models of Ganymede's ambient electron environment. The dashed black line shows the fit from Paranicas et al. (1999) who combined data from the *Energetic Particles Detector* (EPD) and PLS instruments during the G2 and G7 encounters of the moon to constrain the ambient electron differential number flux from $1 \text{ keV} \leq E_0 \leq 1 \text{ MeV}$. The dashed blue line displays J_0 using G2 EPD measurements for electrons at energies from $20 \text{ keV} \leq E_0 \leq 682 \text{ keV}$ as presented by Cooper et al. (2001). These authors also applied the model of Divine and Garrett (1983) to extend these measurements up to energies of $E_0 = 40 \text{ MeV}$, displayed by the solid blue line in Figure 3.

In addition to the curves corresponding to the G2 and G7 Galileo flybys, Figure 3 includes various models of the average ambient differential electron flux expected near Ganymede's orbit (i.e., at a McIlwain parameter of $L = 15$). For energies between $20 \text{ keV} \leq E_0 \leq 100 \text{ MeV}$, the solid purple line uses the GIRE model (Garrett et al., 2003) to calculate $J_0(E_0)$, while the solid green line uses the GIRE2 model (de Soria-Santacruz et al., 2016). Compared to the GIRE model, GIRE2 has an improved agreement with Pioneer and Voyager data obtained within $8 R_J$ of Jupiter and extends to radial distances of $50 R_J$ from the giant planet (compared to $16 R_J$ for the GIRE model). The orange curve extends to even lower energies than GIRE and GIRE2, displaying a fit to the ambient electron population introduced by Jun et al. (2019). This fit combines a Maxwellian distribution at energies $E_0 < 0.11 \text{ keV}$ with a kappa distribution for $E_0 > 0.11 \text{ keV}$. In order to ensure a continuous transition between the kappa distribution and the endpoint of the GIRE curve at $E_0 = 20 \text{ keV}$, we use a kappa factor of 1.45 and a characteristic energy of 70 eV, which are each within the range of values presented by Jun et al. (2019) for the electron distribution near Ganymede. Finally, for comparison purposes, the differential flux of the *thermal* electron population is shown in Figure 3 by the solid yellow line, which displays a Maxwellian distribution with a bulk density of $n_0 = 5 \text{ cm}^{-3}$ and temperature of $T_0 = 300 \text{ eV}$ (Kivelson et al., 2004). Note that the model curves in Figure 3 present an *average* state of the spin-averaged ambient energetic population near Ganymede; that is, each uses a fit to data obtained cumulatively during multiple spacecraft encounters over a decades-long time frame. Further details on the fitting procedures to obtain $J_0(E_0)$ for each of these curves can be found in their respective publications.

For each of the icy Galilean moons, Paranicas et al. (2018) have quantified the change in the radial distance between Jupiter and the point of minimum magnetic field magnitude on the field line to which the moon is connected. Note that for a satellite located at the magnetic equator of a dipole field, this "magnetic distance" is equal to the standard McIlwain L parameter. During Ganymede's orbit around Jupiter, Paranicas et al. (2018) have shown that the moon's magnetic distance varies between 15.0 and $17.4 R_J$ as it travels into and out of the magnetospheric current sheet. Although any variability (e.g., as a function of System III longitude) of the ambient energetic electron distribution near Ganymede is averaged out by the models in Figure 3, the approach of Paranicas et al. (2018) can be used to identify the range in the energetic electron intensity observed by the Galileo EPD. Inspection of Figure 3 in Paranicas et al. (2018) shows that at the two extremes of Ganymede's magnetic distance, the ambient differential energetic electron flux only changes by approximately a factor of 3 (averaged over the entire Galileo mission; see also Jun et al., 2005).

Hence, for this study, we assume the *same* ambient differential flux to investigate electron precipitation patterns onto Ganymede during the G1 and G28 encounters as we used for the G8 flyby (see Figure 3). In doing so, we can dismiss any changes in the surface flux and bombardment patterns between these encounters from being generated by slight discrepancies (of approximately a factor of 3) between the ambient differential fluxes when located within and outside of the Jovian magnetospheric current sheet. This approach therefore allows us to isolate the effect that differences in Ganymede's electromagnetic environment may have on the variability of precipitating energetic electron fluxes. To constrain the electron flux precipitating onto Ganymede, we apply the ambient differential flux obtained from two different fits in Figure 3. For electrons with energies $4.5 \text{ keV} \leq E < 20 \text{ keV}$, we use the kappa fit of Jun et al. (2019), while for electrons with energies $20 \text{ keV} \leq E \leq 100 \text{ MeV}$, we use the GIRE model of Garrett et al. (2003) (see the shaded region following the solid orange and purple curves in Figure 3). We note that at a given energy within the range considered here, slight differences between the analytical fits do exist. However, these discrepancies are within an order of magnitude, and any quantitative changes in the resulting surface fluxes are expected to be minor.

Since each of the models in Figure 3 represents an averaged state of the energetic electron distribution in the undisturbed plasma near Ganymede, we assume that the ambient differential electron flux $J_0(E_0)$ (and hence, the ambient distribution function $f_0(p_0)$, with relativistic electron momentum p_0) is isotropic and homogeneous, and that all electrons stem from this distribution. This assumption is consistent with

measurements from the Galileo EPD in the ambient plasma near Ganymede's orbit (see, e.g., Allioux et al., 2013; Paranicas et al., 1999). Note that in this case, the precipitating electron flux onto a given point of Ganymede is reduced by *at least* a factor of 2 compared to the ambient distribution, since half of those electrons are shadowed by the moon's surface. Once an electron *backtraced* with GENTOO has an "allowed" trajectory (i.e., after it exits the upstream *or* downstream boundary of the hybrid simulation domain), we assign to it an ambient phase space density $f_0(p_0)$ based on the differential flux $J_0(E_0)$ in the undisturbed plasma using the relation

$$f_0(p_0) = \frac{J_0(E_0)}{p_0^2} \quad (1)$$

(see also, e.g., Kollmann et al., 2018; Xiao et al., 2008). In the absence of collisions, Liouville's theorem states that this phase space density is conserved along a dynamical trajectory. Hence, $f_0(p_0)$ in the undisturbed plasma can be used to determine the relativistic electron momentum distribution function on Ganymede's surface $f(p)$. Following the procedure of Xiao et al. (2008), we take moments of this surface distribution function to quantify the flux of energetic electrons onto the moon (see also, e.g., Brice & Mcdonough, 1973; Fatemi et al., 2012; Schulz & Lanzerotti, 2012; Wright & Hadley, 1975).

In summary, electrons are initialized at the surface of Ganymede at a given energy E within the range $4.5 \text{ keV} \leq E \leq 100 \text{ MeV}$ and at a given angle to the surface and are traced backward in time using GENTOO. Each electron that reaches the upstream *or* downstream face of the hybrid simulation domain without first reencountering Ganymede's surface has an "allowed" trajectory. Note that the energy E_0 of an electron in the undisturbed ambient plasma (as it exits the hybrid simulation domain with an allowed trajectory) is *not* necessarily equal to the energy E at which it was initialized. The phase space densities f_0 of "allowed" electrons in the ambient plasma are conserved along their paths as they travel through Ganymede's perturbed electromagnetic environment. Hence, using this surface phase space density $f = f_0$, we calculate the electron flux onto each point of Ganymede.

5. Results

5.1. Energetic Electron Precipitation Onto Ganymede When Located Near the Jovian Magnetic Equator: The G8 Flyby

Figure 4 displays the Jovian magnetospheric energetic electron number flux (left column) and energy flux (right column) onto Ganymede's surface during the G8 flyby. Figures 4a and 4b show surface fluxes for electrons with energies between $4.5 \text{ keV} \leq E \leq 100 \text{ MeV}$, while subsequent panels display the fluxes within three narrower energy ranges: (c, d) $4.5 \text{ keV} \leq E < 450 \text{ keV}$, (e, f) $450 \text{ keV} \leq E < 40 \text{ MeV}$, and (g, h) $40 \text{ MeV} \leq E \leq 100 \text{ MeV}$. The vertical axis displays latitude on the surface, with 90°N the moon's north pole, 0° the equator, and 90°S the south pole. The horizontal axis uses west longitude, which increases when traveling westward across Ganymede's surface. Within the equatorial plane, 0°W is the apex of the sub-Jovian hemisphere (i.e., facing *toward* Jupiter) and 180°W is the apex of the anti-Jovian hemisphere (i.e., facing *away* from Jupiter); 270°W is located in the moon's orbital trailing (ramside) hemisphere, with antipodal longitude 90°W in the leading (wakeside) hemisphere.

Figures 4a and 4b highlight that the pattern of energetic electron precipitation onto Ganymede's surface is strongly partitioned by latitude, with the number flux onto Ganymede's poles enhanced by over 4 orders of magnitude compared to equatorial latitudes, where a "stripe" of reduced flux exists. At the lowest energies, this stripe covers nearly 60% of the moon's surface where nearly *no* electron precipitation occurs, as is visible in Figures 4c and 4d. These distinct regions are separated along Ganymede's OCFB, denoted by a rapid change in flux near midlatitudes. Equatorward of these locations, *backtraced* electrons are initialized within the loss cone of Ganymede's minimagnetospheric field, intersect the surface, and become forbidden. With increasing energy, this equatorial stripe continues to narrow until it finally disappears at energies above $E \approx 40 \text{ MeV}$ (see Figures 4g and 4h). Hence, the separation between open and closed field lines is *not* a sharp boundary for impinging electrons, as they gradually penetrate to more equatorial latitudes with increasing energy. Note that even though precipitation is enhanced along the OCFB, energetic electrons do not significantly contribute to the generation of auroral signatures at Ganymede (Eviatar et al., 2001; McGrath et al., 2013; Paranicas et al., 1999; Payan et al., 2015).

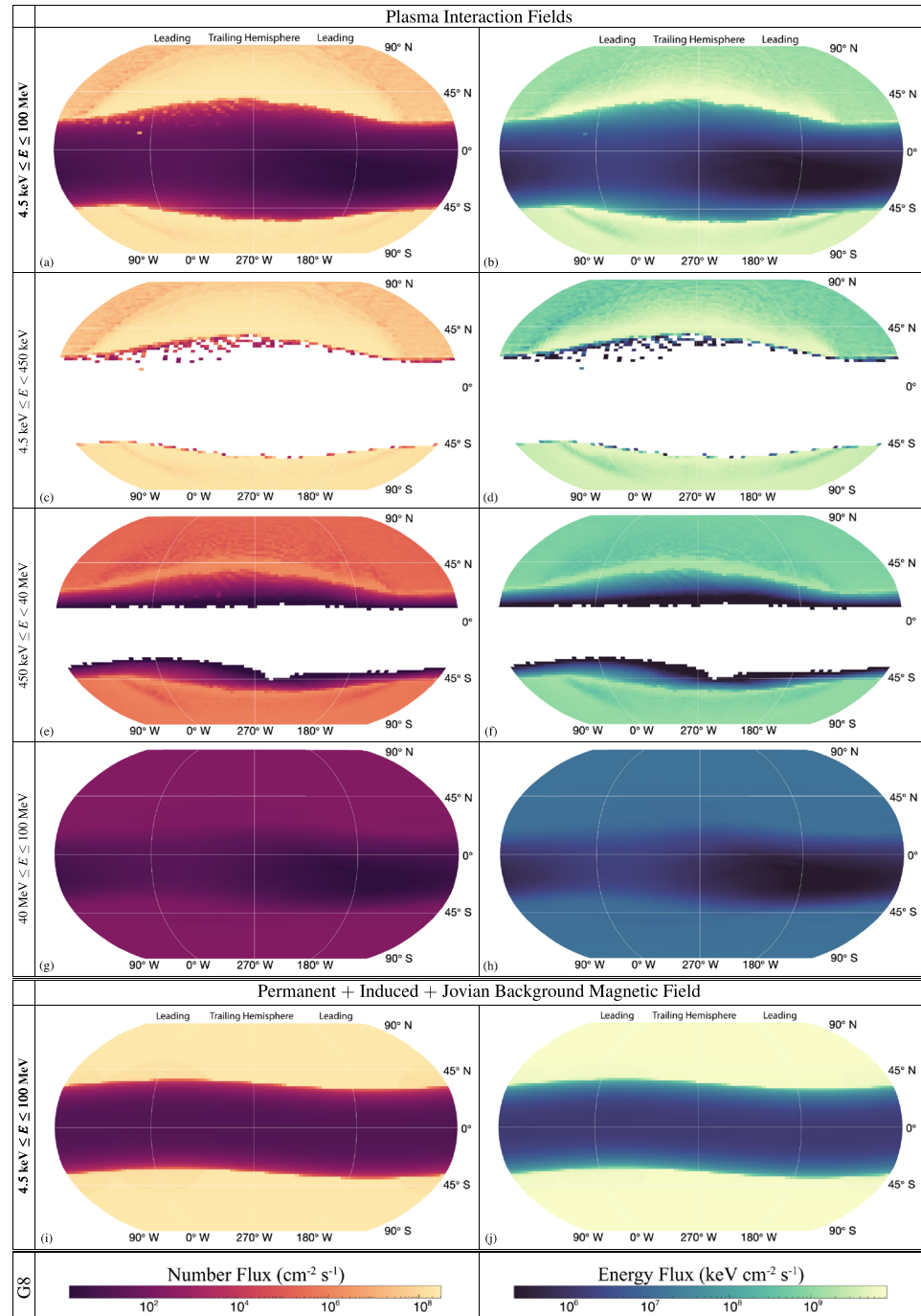


Figure 4. Energetic electron (left column) number and (right column) energy flux onto Ganymede during the Galileo G8 flyby, when the moon was embedded within Jupiter's magnetospheric current sheet. Panels (a), (b), (i), and (j) include fluxes for the entire range of energies considered in this study ($4.5 \text{ keV} \leq E \leq 100 \text{ MeV}$). The remaining panels display a subset of energies from (c, d) $4.5 \text{ keV} \leq E < 450 \text{ keV}$, (e, f) $450 \text{ keV} \leq E < 40 \text{ MeV}$, and (g, h) $40 \text{ MeV} \leq E \leq 100 \text{ MeV}$. Panels (i) and (j) display the electron fluxes when considering only the superposition of Ganymede's permanent and induced magnetic field with the Jovian magnetospheric background field (i.e., *without* considering currents generated by Ganymede's thermal plasma interaction). The locations of Ganymede's leading and trailing hemispheres are given in the top panels. The leading (wakeside) hemisphere is located between 0°W and 180°W longitude with the apex centered at 90°W , while the trailing (ramside) hemisphere is located between 180°W and 0°W with the apex at 270°W . The geographic north and south poles are located at 90°N and 90°S , respectively. White areas denote regions on the surface with zero flux (i.e., where no electrons precipitate in our model).

To constrain the effect of Ganymede's interaction with the thermal plasma on the resulting energetic electron flux patterns, Figures 4i and 4j consider only the superposition of Ganymede's permanent and induced magnetic field with the local Jovian magnetospheric background field during G8. Hence for these panels, electrons are traced *backward* in time through a local electromagnetic environment near Ganymede that is identical to the fields used by Cooper et al. (2001) to estimate electron fluxes onto the moon's surface. Figures 4i and 4j highlight that without including the electromagnetic perturbations generated by Ganymede's interaction with the thermal plasma, electron precipitation is nearly uniform with longitude. Within the moon's polar caps, the bombardment is nearly homogeneous with a number flux of $3 \cdot 10^8 \text{ cm}^{-2} \text{ s}^{-1}$. Similar to Figure 4a with plasma currents included, the flux still rapidly decreases across the OCFB, reduced by more than 4 orders of magnitude within a "stripe" surrounding Ganymede's equatorial region. Figures 4i and 4j show that this feature is slightly "wavy" in longitude, due to the (small) inclination of Ganymede's magnetic moment against the orientation of the magnetospheric background field during G8 (see, e.g., Figure 1 or Jia et al., 2008). Analogous "waviness" in energetic particle precipitation patterns has also been identified at Callisto (Liuzzo et al., 2019a, 2019b) as well as Europa (Breer et al., 2019).

Without considering Ganymede's interaction with the thermal magnetospheric plasma, electrons approach Ganymede poleward of the OCFB and have nearly uniform access to the moon's high-latitude surface, resulting in an average polar electron number flux of $3 \cdot 10^8 \text{ cm}^{-2} \text{ s}^{-1}$ (see Figure 4j). These fluxes agree with previous estimations provided by, for example, Frank et al. (1997), Delitsky and Lane (1998), and Cooper et al. (2001), who assumed that the incident electron flux is homogeneous at high latitudes. However, comparison of Figure 4a with Figure 4i highlights the important role that Ganymede's interaction with the thermal magnetospheric plasma plays in energetic electron bombardment. In the trailing (ramside) hemisphere near 270°W longitude, the impinging magnetospheric plasma compresses Ganymede's magnetic field, thereby shifting the boundary between the open and closed field lines toward more polar latitudes. Hence, the equatorial region of reduced electron fluxes is broader when including Ganymede's plasma interaction, extending to approximately 40°N and 50°S . In this hemisphere, the stripe spans a total of nearly 90° in latitude, compared to the case without the perturbed electromagnetic fields, where this stripe spans only 60° (cf. Figures 4a and 4i). In the leading hemisphere, however, Ganymede's interaction with the Jovian magnetospheric plasma drags the OCFB slightly equatorward (e.g., Saur et al., 2015). As a result, the equatorial stripe with reduced electron fluxes displays a longitudinal asymmetry, becoming narrower in the leading hemisphere where it spans only 55° in latitude (again compared to approximately 60° in the case without Ganymede's plasma interaction).

In addition, Figure 4a illustrates that Ganymede's thermal plasma interaction causes the flux onto the moon's poles to be remarkably inhomogeneous. A nonuniform "band" of enhanced flux, located in the orbital trailing hemisphere near 40°N latitude, extends toward the geographic north pole. Within this band, the number flux reaches values of $3 \cdot 10^8 \text{ cm}^{-2} \text{ s}^{-1}$ (yellow hues in Figure 4a). This feature is centered around 270°W longitude and reaches into Ganymede's sub-Jovian and anti-Jovian flanks beyond 0°W and 180°W toward the leading hemisphere. Beyond these locations, however, the flux decreases by more than an order of magnitude, locally reaching values of $1 \cdot 10^7 \text{ cm}^{-2} \text{ s}^{-1}$ (orange hues in Figure 4a). Precipitating electrons between $4.5 \text{ keV} \leq E < 40 \text{ MeV}$ are responsible for generating this nonuniform polar flux pattern: even though the high-latitude flux from the highest energy electrons at $40 \text{ MeV} \leq E \leq 100 \text{ MeV}$ is nearly homogeneous, the rapid decrease in the ambient differential flux with increasing energy causes the contribution of the highest energy electrons to be minimal within the polar caps (cf. Figure 4a with Figures 4c and 4g or Figure 4b with Figures 4d and 4h).

Similarly, a second band poleward of the OCFB at southern latitudes between 55°S and 65°S is also present (see Figure 4b). This feature in the southern hemisphere is less distinct than its northern counterpart: due to their larger bounce periods at a given energy, electrons mirroring in Jupiter's southern hemisphere are, on average, displaced azimuthally at greater distances from Ganymede compared to their counterparts that mirror in Jupiter's northern hemisphere (see Figure 2). Hence, electrons precipitating onto the southern polar cap are able to access larger swaths of Ganymede's high-latitude surface (poleward of approximately 60°) than those precipitating onto the northern polar cap (see also Liuzzo et al., 2019a). This generates a slight north/south asymmetry in the polar flux that is most noticeable in the energy flux pattern of Figure 4b. The resulting high-latitude electron number flux is nearly an order of magnitude greater than the average

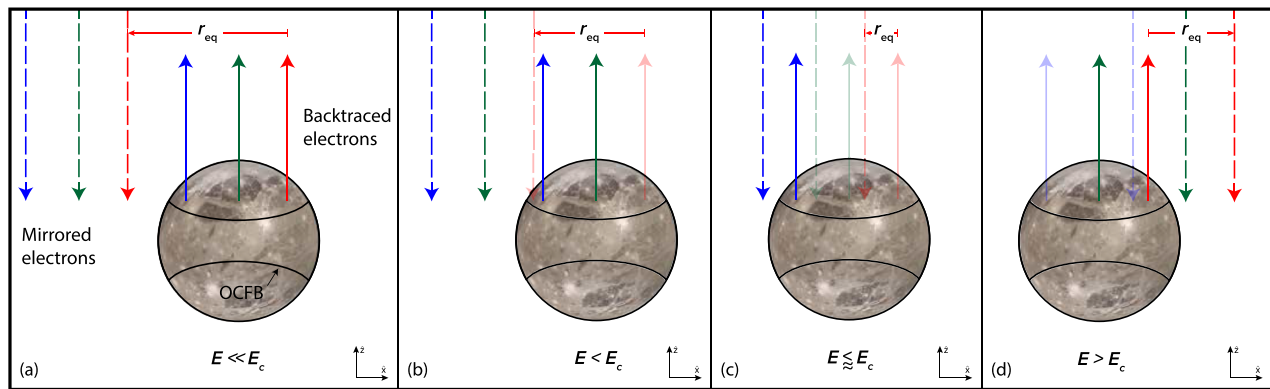


Figure 5. Schematic explaining the band of enhanced electron flux in Ganymede’s trailing hemisphere between 30°N and 60°N latitude (see also Figure 4). Red, green, and blue lines denote example trajectories of the guiding centers of three electrons initialized at Ganymede’s surface and traced backward in time. Dashed lines show these electrons after they travel through Jupiter’s magnetospheric field, mirror, and return to the moon, displaced azimuthally by r_{eq} (see section 4 for further details). Opaque lines represent electrons with allowed trajectories, while translucent lines denote forbidden trajectories. These three electrons are initialized at four distinct energies E with respect to the critical energy $E_c \approx 2$ MeV at which their drift velocity is in resonance with Ganymede’s orbital velocity: (a) $E \ll E_c$, (b) $E < E_c$, (c) $E \approx E_c$, and (d) $E > E_c$. The electrons’ initial energy increases from left to right in the panels. Ganymede image credit: NASA.

energetic *ion* flux onto the same region during G8 (on the order of $10^7 \text{ cm}^{-2} \text{ s}^{-1}$ for hydrogen, oxygen, and sulfur combined; see Poppe et al., 2018).

Two mechanisms contribute to the generation of these bands with enhanced energetic electron flux in Ganymede’s high-latitude trailing hemisphere, the first of which is Ganymede’s interaction with the ambient magnetospheric plasma. This interaction reduces the convection speed of the Jovian magnetospheric field lines in the immediate vicinity of the moon, thereby generating perturbations in the ambient electromagnetic environment. Poppe et al. (2018) have shown that for energetic *ions* with gyroradii $r_g \ll R_G$, this interaction results in a flux enhancement along the entire upstream boundary of Ganymede’s Alfvén wings and a depletion in ion flux at the downstream boundary (see Figure 7 in that work). The resulting ion precipitation pattern onto the polar surface is inhomogeneous: in the trailing hemisphere, a band of flux forms near the OCFB that is enhanced by up to an order of magnitude compared to more polar latitudes, while in the leading hemisphere, the energetic ion fluxes near the OCFB are further reduced. Figures 4a and 4b reveal that similar patterns of enhanced energetic *electron* fluxes form as well. In the trailing hemisphere, the reduced velocity of the Jovian magnetospheric field lines causes enhanced electron precipitation poleward of the OCFB, where electrons have unrestricted access to Ganymede’s high-latitude surface. At Callisto, Liuzzo et al. (2019a) have identified similar features in the dynamics of energetic electrons; in locations where the moon’s Alfvén wings are “anchored” to Callisto’s surface, energetic electron bombardment is enhanced in the trailing hemisphere compared to in the leading hemisphere.

The second mechanism contributing to these bands of enhanced energetic electron flux is illustrated in Figure 5. This schematic displays the net guiding center motion of three electrons (red, green, and blue lines), each at four select energies (Figures 5a–5d), which are initialized near Ganymede and traced backward in time. Note that the gyroradius of an electron in the undisturbed plasma near Ganymede becomes comparable to the moon’s radius above energies of $E \approx 10$ MeV; that is, this occurs well above the critical energy $E \gg E_c \approx 2$ MeV, and this case is not displayed in Figure 5. For simplicity, Figure 5 considers the electrons’ motion through *uniform* fields, that is, neglecting the effect of Ganymede’s permanent and induced field as well as the interaction with the ambient thermal plasma on the dynamics of energetic electrons. However, the process described below occurs in the case of locally inhomogeneous electromagnetic fields as well.

In GENTOO, *backtraced* electrons with $E \ll E_c$ are displaced azimuthally toward upstream by a distance $|r_{eq}|$ after traveling through the magnetospheric field of Jupiter, mirroring, and returning to the moon. The three electrons (solid lines) visible in Figure 5a are displaced far enough from Ganymede after mirroring and then returning (dashed lines) that they all have “allowed” trajectories. Hence, each of these electrons at $E \ll E_c$ is able to contribute to the surface flux at their injection point.

With increasing energy such that $E < E_c$ (Figure 5b), the absolute value of the electrons' azimuthal displacements $|r_{eq}|$ decreases; that is, although they still travel toward upstream while bouncing, they now return closer to the moon than in Figure 5a. One of these electrons (initialized in Ganymede's leading hemisphere; red line) intersects the moon after mirroring and is forbidden, while the two remaining electrons (green and blue lines) still have allowed trajectories. At larger energies such that $E \lesssim E_c$ (Figure 5c), the azimuthal displacement is $|r_{eq}| < R_G$. In this case, *only* the electron initialized just poleward of the OCFB in Ganymede's trailing hemisphere (blue line) has an allowed trajectory and can contribute to energetic electron flux. The other two electron trajectories are forbidden. Thus, with increasing energy of the backtraced electrons (but while still remaining *below* the critical energy), the final regions on Ganymede's surface that remain "accessible" to electrons are preferentially located in the moon's *trailing* hemisphere, just poleward of the OCFB. Note again that at these energies (i.e., $E \ll 40$ MeV), no electrons are able to penetrate the closed field line region to bombard the equator (see Figures 4c–4f).

For energies E just above the critical energy $E_c \approx 2$ MeV, the first high-latitude region that becomes accessible to backtraced electrons is near Ganymede's OCFB in the *leading* hemisphere. With increasing energy above E_c (Figure 5d), additional regions located at higher latitudes and farther into the moon's flanks toward the anticorotation direction subsequently become accessible to electrons (e.g., the red and green lines in Figure 5d). Indeed, band-like regions of enhanced electron precipitation form in Ganymede's high-latitude, leading hemisphere at energies $E > E_c$ (maps of electron precipitation at each discrete energy considered in this study can be found in the supporting information). If the differential electron flux in the ambient plasma near Ganymede remained constant with increasing energy, a band of enhanced flux would be present in the *leading* hemisphere at latitudes poleward of the OCFB in Figure 4, in addition to the band present in the high-latitude *trailing* hemisphere. However, since the ambient electron flux decreases multiple orders of magnitude with increasing energy (see Figure 3), the precipitation of electrons with $E > E_c$ onto these regions does *not* result in a noticeable flux enhancement in Ganymede's leading hemisphere.

A process similar to the one described above is even more pronounced at those moons in the Saturnian and Jovian systems, which do not possess strong intrinsic magnetic fields (e.g., Krupp et al., 2009; Roussos et al., 2013). Consider an example in the forward-tracing approach where the bounce periods of electrons are much faster than the convection time of a magnetospheric flux tube across a moon's surface. Electrons trapped on that field line with energies *just below* the local critical energy (that travel azimuthally along the corotation direction) precipitate within a narrow region surrounding the apex of the *trailing* hemisphere as the flux tube initially comes into contact with the moon (Paranicas et al., 2001; Patterson et al., 2012). Bouncing electrons with energies even further below this critical energy (and thus with longer bounce periods; e.g., Thomsen & Van Allen, 1980) are not only able to precipitate onto this point but also bombard concentric locations that extend into the flanks and toward more polar latitudes of the surface (see, e.g., Krupp et al., 2013). This behavior generates a distinct "bull's-eye" precipitation pattern in the moons' trailing hemispheres (for electrons with energies $E < E_c$; e.g., Dalton et al., 2013; Paranicas et al., 2001). Such patterns also form in the leading hemispheres of these icy moons: bombardment of electrons with energies E just above E_c is restricted to a narrow region surrounding the *leading* apex. This behavior is responsible for generating the "lens" feature seen on Mimas, Tethys, and Dione (e.g., Nordheim et al., 2017; Paranicas et al., 2014) as well as an additional "bull's-eye" in the electron precipitation pattern at Europa's leading surface (Nordheim et al., 2018).

The biggest difference between these icy moons and Ganymede, however, is the presence of a strong permanent magnetic field that complicates this (somewhat simplified) description of electron precipitation. Without Ganymede's intrinsic field, electrons would similarly be able to precipitate near the equator to form a familiar bull's-eye flux pattern. However, nearly all electrons are prohibited from ever reaching Ganymede's equatorial surface; Figure 4 shows that the closed field lines surrounding the equator *drastically* reduce the energetic electron flux here compared to more polar latitudes. Indeed, even electrons at energies well above E_c *cannot* penetrate the closed field line region to access the equator (see Figures 4c–4f), thereby hindering the formation of a bull's-eye pattern at equatorial latitudes of Ganymede.

In other words, the closed field line region generated by Ganymede's permanent field "carves out" a depletion region from the bull's-eye pattern that would be expected at an inert moon. This depletion is located *exactly* where the electron fluxes onto inert moons would be maximized. The only hint of any remaining bull's-eye signature in the electron flux onto Ganymede's surface occurs at latitudes poleward of the OCFB,

Table 1

Energetic Particle Fluxes Onto Ganymede's Surface When the Moon Is Located Near the Center of Jupiter's Magnetospheric Current Sheet (i.e., for the Galileo G8 Encounter)

| | Electrons (this study) | Electrons (Cooper et al., 2001) | Ions (Cooper et al., 2001) | Ions (Poppe et al., 2018) |
|--|--|--|--|--|
| Energy range (MeV) | $4.5 \cdot 10^{-3} \leq E \leq 1 \cdot 10^2$ | $2 \cdot 10^{-2} \leq E \leq 4 \cdot 10^1$ | $2 \cdot 10^{-2} \leq E \leq 1 \cdot 10^2$ | $1 \cdot 10^{-3} \leq E \leq 1 \cdot 10^1$ |
| Polar caps | | | | |
| Number flux ($\text{cm}^{-2} \text{s}^{-1}$) | $1.2 \cdot 10^8$ | $3.1 \cdot 10^7$ | $8.8 \cdot 10^6$ | $3.9 \cdot 10^7$ |
| Energy flux ($\text{keV cm}^{-2} \text{s}^{-1}$) | $3.0 \cdot 10^9$ | $3.4 \cdot 10^9$ | $2.0 \cdot 10^9$ | $1.6 \cdot 10^9$ |
| Equator | | | | |
| Number flux ($\text{cm}^{-2} \text{s}^{-1}$) | $3.3 \cdot 10^3$ | N/A | $1.0 \cdot 10^5$ | $3.6 \cdot 10^6$ |
| Energy flux ($\text{keV cm}^{-2} \text{s}^{-1}$) | $4.1 \cdot 10^6$ | N/A | $2.6 \cdot 10^8$ | $2.8 \cdot 10^8$ |

Note. All fluxes are averaged across the corresponding surface region; the flux onto any given point within each region may substantially vary from the values provided here (cf. Figure 4). Energetic electron fluxes into Ganymede's polar caps (poleward of 60° latitude) and equatorial region (latitudes equatorward of 20°) are provided to facilitate a direct comparison with energetic ion fluxes presented in Cooper et al. (2001) and Poppe et al. (2018). The given ion fluxes are summed over the three dominant energetic ion species near Ganymede's orbital location (hydrogen, oxygen, and sulfur), presented here as a total average ion flux. The lower limit to the energy ranges for the equatorial fluxes provided by Cooper et al. (2001) is the (analytical) Størmer cutoff energy for each species.

manifesting as the longitudinally asymmetric band of enhanced electron flux in the trailing hemisphere visible in Figure 4. Similar signatures of a decreasing energetic electron flux with increasing latitude poleward of the OCFB have been observed by Galileo in multiple EPD electron channels during the G2 encounter (see Figure 4 of Eviatar et al., 2001). The presence of these bands with enhanced electron flux likely generate an asymmetric weathering pattern of Ganymede's high-latitude surface and may partially contribute to the nonuniform ionization of its atmosphere (albeit to a lesser degree than by electrons with energies $E \ll 4.5$ keV; cf. Carnielli et al., 2019). Hence in summary, Ganymede's interaction with the ambient plasma and the rapid bounce times of electrons near Ganymede (e.g., Figure 5) both contribute to the generation of these high-latitude "bands" of enhanced electron flux along Ganymede's high-latitude, trailing hemisphere surface.

Cooper et al. (2001) calculated the Størmer cutoff energy for electrons in Ganymede's permanent field to be on the order of 100 MeV. Indeed, Figures 4c–4f show that *no* electrons at energies from $4.5 \text{ keV} \leq E < 40 \text{ MeV}$ can precipitate within the stripe surrounding Ganymede's equatorial region. Electrons at these energies are unable to penetrate the equatorial closed field line region of Ganymede's dipole to access these surface locations. However, Figures 4g and 4h show that electrons at energies $E \geq 40 \text{ MeV}$ *can* penetrate the closed field lines and contribute to a nonnegligible equatorial particle flux.

Although Cooper et al. (2001) did not calculate equatorial surface fluxes for electrons of any energy, they estimated the fluxes of *ions* with energies $E \leq 100 \text{ MeV}$ (by considering *only* the magnetic field generated by the superposition of Ganymede's permanent dipole with the Jovian background field at altitudes below $1 R_G$). Similarly, Poppe et al. (2018) calculated the number fluxes of ions between $1 \text{ keV} \leq E \leq 10 \text{ MeV}$ onto Ganymede's surface for the perturbed electromagnetic fields during the Galileo G8 encounter. Hence, we can compare values of energetic ion fluxes from these previous studies with the electron fluxes in Figure 4. This comparison is presented in Table 1. On average, Cooper et al. (2001) estimated equatorial ion number fluxes of $5.9 \cdot 10^3 \text{ cm}^{-2} \text{ s}^{-1}$ for hydrogen, $3.7 \cdot 10^4 \text{ cm}^{-2} \text{ s}^{-1}$ for oxygen, and $5.8 \cdot 10^4 \text{ cm}^{-2} \text{ s}^{-1}$ for sulfur. Poppe et al. (2018) found similar ion number fluxes equatorward of 20° latitude for each of these species (see Figures 9c–9e of that study). These number fluxes for each energetic ion species are comparable to the average equatorial electron number flux within 20°N/S latitude during G8 of $3.3 \cdot 10^3 \text{ cm}^{-2} \text{ s}^{-1}$ (see Figure 4a and Table 1). Indeed, even locally, the proton energy flux onto Ganymede's trailing apex reported by Cooper et al. (2001) is similar to the electron energy flux onto this point visible in Figure 4b of $2 \cdot 10^6 \text{ keV cm}^{-2} \text{ s}^{-1}$ (cf. with Figure 9b of that study). However, Table 1 illustrates that the total energy flux onto the equator from energetic ions (i.e., summed over the three ion species) is nearly 2 orders of magnitude greater than the energetic electron flux, with even larger differences between the number fluxes. Regardless, Figure 4 and Table 1 demonstrate that the precipitation of energetic electrons onto Ganymede's equatorial surface plays an important role in contributing to the net charged particle flux onto this region.

In addition to the differences at high latitudes in the energetic electron flux when considering Ganymede's interaction with the ambient magnetospheric plasma, comparison of Figures 4a and 4b with Figures 4i and

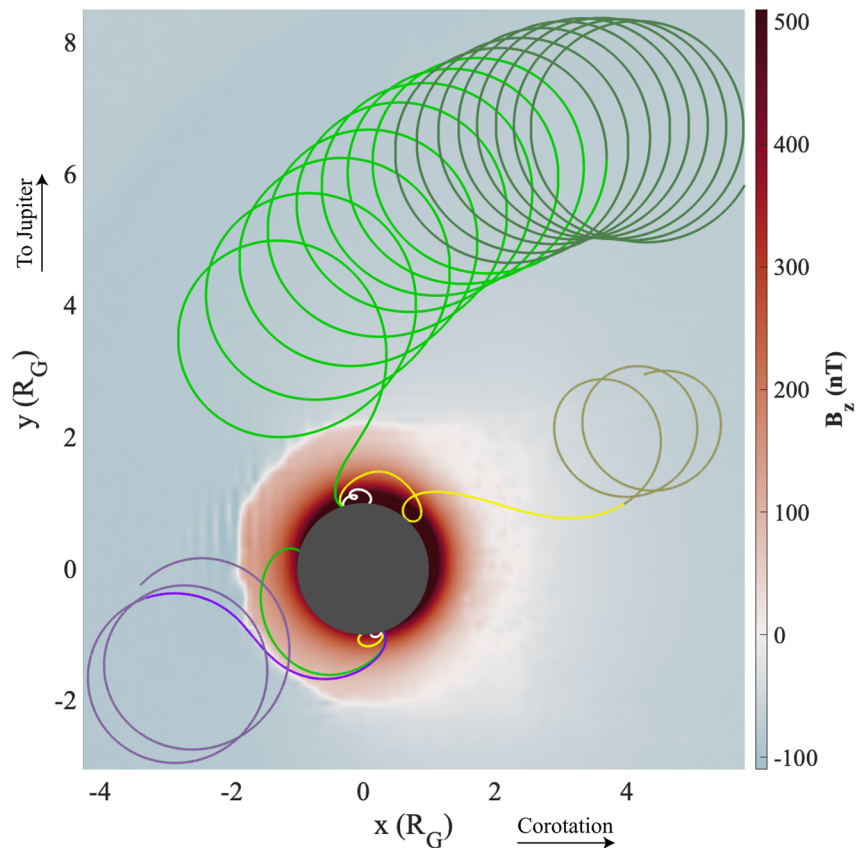


Figure 6. B_z component of the magnetic field in Ganymede's equatorial ($z = 0$) plane from hybrid modeling of the Galileo G8 encounter, with select *backtraced* electron trajectories projected onto this plane. The intersection of Ganymede with the equatorial plane is denoted by the gray circle. Three separate electron starting energies are shown: (white) $E = 38$ MeV, (yellow) $E = 65$ MeV, and (green and purple) $E = 100$ MeV. Desaturated hues along the trajectories denote the points at which electrons have traveled north or south of Ganymede (i.e., the location where $|z| > 1 R_G$). See text for discussion on the electrons' starting positions and initial velocities.

4j shows that this interaction generates a nonuniformity with longitude near the equator in the electron flux pattern. Near 0°W , the equatorial fluxes are *more than an order of magnitude larger* than the fluxes at antipodal points surrounding 180°W . These enhanced fluxes cover most of the moon's equatorial sub-Jovian surface (starting near longitudes of 270°W in the trailing hemisphere and extending westward into the leading hemisphere beyond 0°W toward 90°W), whereas the region with reduced flux is nearly entirely located in the anti-Jovian hemisphere. Previous studies that have considered the effect of Ganymede's thermal plasma interaction on energetic *ions* have demonstrated a similar but *opposite* longitudinal asymmetry. The ion flux patterns display a local maximum in the leading, anti-Jovian hemisphere and a local minimum in the trailing, sub-Jovian hemisphere (e.g., Fatemi et al., 2016; Plainaki et al., 2015). Such an asymmetric pattern in the *ion* flux was shown to be mainly caused by the clockwise sense (viewed from a location above Ganymede) of the drift motion of quasitrapped ions as they orbit Ganymede in the local minimagnetospheric field and continuously precipitate onto the surface (Poppe et al., 2018).

To identify the cause of the longitudinal asymmetry in the equatorial *electron* fluxes, Figure 6 displays the trajectories of select electrons as they are traced backward in time through the moon's perturbed electromagnetic environment. The B_z component of the magnetic field in Ganymede's equatorial ($z = 0$) plane during the Galileo G8 flyby is also included. Blue shades correspond to regions where $B_z < 0$ (i.e., where the magnetic field has a southward component), reds denote $B_z > 0$ (where the field is northward), and white shows locations where $B_z = 0$. Trajectories of seven *backtraced* electrons are projected onto this plane, corresponding to three different starting energies: (white) $E = 38$ MeV, (yellow) $E = 65$ MeV, and (green and purple) $E = 100$ MeV. The three electrons in Ganymede's sub-Jovian ($y > 0$) hemisphere are initialized on the surface at 20°S latitude and 345°W longitude, that is, in the hemisphere opposite to the location of *minimum*

electron flux onto Ganymede's surface (see Figure 4). The velocity vector of each electron is initialized at an angle of $v_\theta = 120^\circ$ from local zenith and tilted $v_\phi = 270^\circ$ against local north. Conversely, in the opposite hemisphere ($y < 0$), the electrons represented by the white, yellow, and green trajectories are launched at the same latitude and at an identical angle from local zenith and local north but at 165°W longitude (i.e., within the region of minimum flux). Finally, the electron denoted by the purple trajectory is also launched in this hemisphere at a latitude of 20°S and longitude of 165°W but with its azimuthal velocity angle increased by 5° (i.e., $v_\phi = 275^\circ$).

As discussed earlier, electrons with energies below $E \approx 40$ MeV are unable to precipitate onto Ganymede's low-latitude surface (see Figure 4). Indeed, Figure 6 shows that the two *backtraced* electrons initialized at $E = 38$ MeV (white trajectories) are unable to exit the equatorial closed field line region; they reencounter Ganymede's surface and become "forbidden." However, even possessing an energy above 40 MeV is not sufficient to ensure that an electron will have an "allowed" trajectory: it must still leave the moon's inhomogeneous electromagnetic environment without intersecting the surface (note that at these energies, the electrons' azimuthal displacements $|r_{\text{eq}}|$ after mirroring exceed the size of the hybrid simulation domain). Even the yellow ($E = 65$ MeV) and green ($E = 100$ MeV) electron trajectories initialized in the anti-Jovian hemisphere still impact the moon with forbidden trajectories.

Figure 6 reveals that the asymmetric equatorial flux pattern stems from the electrons' gyration around, and drift within, Ganymede's minimagnetospheric field. Within approximately $2R_G$ of the moon, the magnetic field is oriented northward ($B_z > 0$; red shades in Figure 6). Even at the highest energies considered ($E = 100$ MeV), electrons initialized on Ganymede's surface within this field have gyroradii $r_g \lesssim R_G$. Hence, *backtraced* electrons initially gyrate and drift through the minimagnetosphere in a *clockwise* direction (as viewed from above). This net motion results in a larger number of "allowed" electrons in the sub-Jovian hemisphere compared to the anti-Jovian hemisphere, generating the longitudinal asymmetry visible in Figure 4. Consider the yellow ($E = 65$ MeV) and green ($E = 100$ MeV) electrons in Figure 6 initialized in the anti-Jovian hemisphere ($y < 0$; near 180°W longitude): as they travel in a clockwise direction around Ganymede, their gyration causes them to impact the moon before completing a full gyroperiod.

Alternatively in the sub-Jovian hemisphere ($y > 0$; near 0°W), while the yellow electron drifts around Ganymede, it avoids impacting during its first gyration as the moon's surface curves away from the electron's path. During its second gyroperiod, the particle travels *outside* of Ganymede's minimagnetosphere, characterized by a reversal in the direction of the magnetic field from northward inside the minimagnetosphere (red hues in Figure 6) to southward outside of it (blue hues). During this transition, the electron's gyroradii grows as the electron becomes "demagnetized" while passing through the region of reduced $|B_z|$ (white hues), thereby allowing the particle to travel even farther from Ganymede along a quasilinear trajectory. After leaving this "booster" region where the electron's gyroradius increases, the electron exits the minimagnetosphere and enters the region of $B_z < 0$. At this location downstream of Ganymede, the electron's sense of gyration reverses, becoming counterclockwise. The net azimuthal drift motion of this $E = 65$ MeV, *backtraced* electron in the ambient Jovian magnetospheric field is along the corotation direction (for energies well above the critical energy of $E_c \approx 2$ MeV). Hence, as the electron continues its counterclockwise gyration, it drifts away from Ganymede and exits the downstream boundary of the hybrid simulation with an allowed trajectory. The green electron initialized at this same sub-Jovian location experiences a similar fate. However, due to the larger initial gyroradius of this $E = 100$ MeV electron, it almost immediately gyrates into the region of reduced magnetic field. Again, its gyroradius is "boosted," allowing the electron to travel along a nearly linear trajectory until it exits Ganymede's minimagnetosphere where its sense of gyration flips, and it begins drifting toward downstream.

On the other side of Ganymede (at 165°W longitude in the anti-Jovian hemisphere), the purple electron also avoids impacting the moon. This 100 MeV electron's large initial gyroradius allows it to almost immediately travel through regions with reduced $|B_z|$ (further enhancing its gyroradius and facilitating its escape), exit the minimagnetosphere during its first complete gyration, and avoid intersecting the moon's surface. Once this electron exits the minimagnetosphere and its sense of gyration reverses, it travels along a new gyrocircle; the point to which the electron returns after completing a single gyroperiod is no longer close to its injection point on Ganymede's surface. Rather, the electron returns near the location where it exited the moon's minimagnetosphere. In the case of the electron with the purple trajectory, this described behavior prevents the particle from ever reencountering Ganymede's surface, resulting in an allowed trajectory. Note

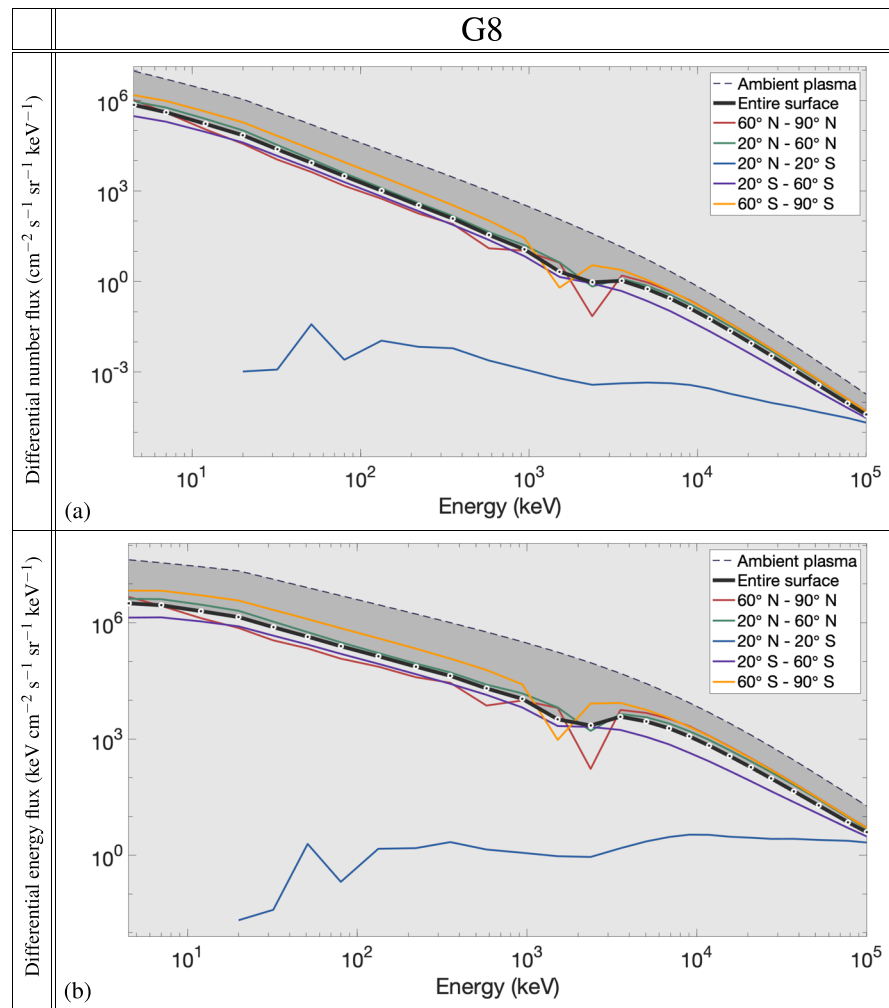


Figure 7. Average precipitating differential electron (a) number and (b) energy flux during the G8 flyby onto (black lines) Ganymede's entire surface as well as (colored lines) five distinct latitude bins. Dashed lines denote the ambient differential flux near Ganymede (i.e., in the unperturbed plasma; see also the orange and purple curves in Figure 3). Shaded regions highlight the differences between the ambient flux and the average global precipitating flux. White points denote the center of the 26 discrete energy bins at which electrons are initialized in the GENTOO simulations. Note that electrons with energies $E < 20$ keV are unable to precipitate equatorward of 20° N/S latitude.

that near the end of its trajectory, the purple electron appears to again pass through the region of reduced $|B_z|$ and reenter Ganymede's minimagnetosphere, where its sense of gyration would reverse. However, this electron is nearly $10 R_G$ north of the moon at this position and remains well outside of Ganymede's minimagnetosphere. Finally, although the green and purple electrons are initialized at the same point with the same energy (100 MeV), the slight 5° difference between their initial velocity vectors prevents the green electron from entering the gyroradius “booster” region. Hence, it does not exit the minimagnetosphere, maintains its clockwise sense of gyration, and intersects the moon's surface becoming forbidden.

In a forward-tracing scenario, electrons above the critical energy $E_c \approx 2$ MeV travel azimuthally along the anticorotation direction and approach Ganymede's leading hemisphere. As these electrons enter the moon's minimagnetosphere, they experience a reversal in the magnetic field direction, their sense of gyration flips, and they drift around Ganymede in a counterclockwise direction (when viewed from above). The combination of this counterclockwise drift motion and the reversal of the electrons' gyration preferentially directs these particles to bombard the equatorial leading, sub-Jovian hemisphere. This behavior is well illustrated by the yellow and green electrons with allowed trajectories in Figure 6. Accordingly, the least “accessible” location of Ganymede's equatorial surface is near the trailing, anti-Jovian hemisphere. In order to reach this region, an electron at these energies would either need to complete a nearly full orbit around Ganymede

(without gyrating into the surface) or approach from above/below the moon (without first impacting at a more polar latitude), as in the case for the purple trajectory in Figure 6. The result of this behavior manifests as a longitudinally asymmetric flux of energetic electrons onto Ganymede's equatorial surface as visible in Figure 4.

Figure 7 displays the average precipitating electron differential (panel a) number and (panel b) energy flux onto Ganymede during the G8 encounter. White circles denote the center of each energy bin at which *back-traced* electrons are initialized. The solid black curves display the differential fluxes averaged over the entire surface, whereas the colored curves correspond to separate latitude ranges: polar regions between 60° and 90° (red) north and (orange) south latitude, intermediate regions from 20–60° (green) north and (purple) south latitudes, and (blue) the equator between 20°N and 20°S. For comparison, the dashed line in each panel displays the ambient electron differential number and energy flux in moon's undisturbed plasma environment (see also Figure 3). This figure reveals that at nearly all energies, the flux of electrons that precipitate onto Ganymede's surface is reduced by at least an order of magnitude compared to the ambient electron flux. On average, the precipitating differential number flux spans more than 10 orders of magnitude between the lowest (4.5 keV) and highest (100 MeV) energies, with a range in the differential energy flux of nearly 6 orders of magnitude, identical to the decreases of the ambient fluxes.

At intermediate and high latitudes, the precipitating electron number and energy fluxes remain close to the global average (black curve), gradually decreasing with increasing energy. However near the equator (blue lines), the efficiency of Ganymede's magnetic field in shielding incoming electrons is immediately evident in Figure 7. Below energies of $E \leq 20$ keV, *no* electrons are able to precipitate equatorward of 20°N/S (see also Figure 4). Even for energies between $20 \text{ keV} \leq E \leq 10 \text{ MeV}$, the flux here is still reduced by multiple orders of magnitude compared to higher latitudes. Figure 7 also shows that while the general trend of the equatorial number flux decreases, the energy flux remains approximately constant as a function of energy; at $E = 100 \text{ MeV}$, the flux is only slightly below the global average (cf. the blue curves in each panel). In other words, the combination of Ganymede's magnetic field as well as the moon's interaction with the ambient electromagnetic environment provide little to no shielding of the surface from bombardment of $E > 100 \text{ MeV}$ (i.e., cosmic ray) electrons when the moon is located near the center of Jupiter's magnetospheric current sheet. Bombardment of high-energy cosmic ray ions has recently been shown to play an important role in the irradiation patterns of Europa (Nordheim et al., 2019) and is likely to affect Ganymede's surface ice as well.

An additional feature of these curves for the G8 encounter is visible near the critical energy $E_c \approx 2 \text{ MeV}$, where the differential fluxes are reduced even further below the general, power law spectral decrease visible elsewhere. These dips are caused by the reduced access of electrons with energies $E \approx E_c$ to Ganymede's surface since at these energies, a backtraced electron has the largest number of “attempts” (during its multiple consecutive bounces) to intersect the moon's surface and become “forbidden.” Hence, near this critical energy in a forward-tracing scenario, the only location where electrons precipitate is just poleward of the OCFB (see Figures 2 and 5 or Figure S1); elsewhere, the fluxes are substantially reduced causing a decrease in the averaged fluxes near E_c . The energy where this depletion occurs is not the same for electrons in Ganymede's northern (red lines) and southern (orange lines) hemispheres, resulting from the slight differences in their bounce times and azimuthal displacements at a given energy (see also Figure 2). Hence, the dip in the globally averaged flux is broader (i.e., spread over a larger energy range) than for any single latitudinal band on the surface. The asymmetry in the electrons' bounce times also causes a slight difference between the northern and southern polar fluxes, with fluxes onto the south pole exceeding those onto the north for energies below $E \approx 10 \text{ MeV}$ by up to an order of magnitude (at the lowest energies).

5.2. Energetic Electron Precipitation Onto Ganymede When Located Far From the Jovian Magnetic Equator: The G1 and G28 Flybys

Having quantified the surface flux when Ganymede is embedded within Jupiter's current sheet, we now analyze how the bombardment patterns change with the moon located outside of the sheet at large magnetic latitudes. In order to disregard any potential differences in the flux maps as being generated by (slight) changes in the ambient energetic electron distribution, we assume the same distribution as during G8 (i.e., using the “Maxwellian + Kappa” and “GIRE” curves in Figure 3).

Figures 8 and 9 display the energetic electron number and energy flux onto Ganymede's surface for the G1 and G28 flybys, respectively. These encounters occurred when Ganymede was located at large magnetic latitudes, far above (G1) or below (G28) the center of Jupiter's magnetospheric current sheet. The

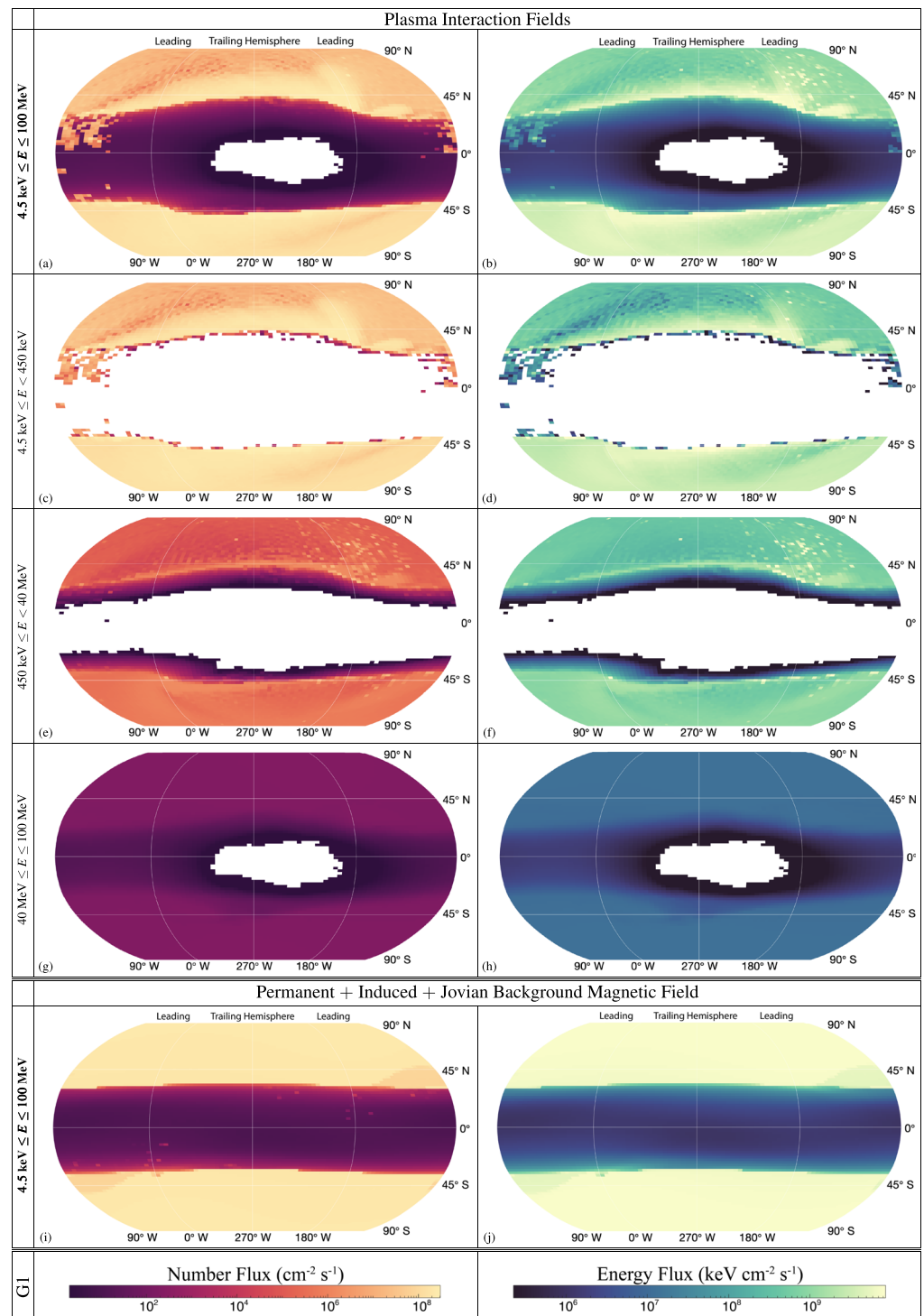


Figure 8. Projection of the energetic electron (left column) number and (right column) energy flux onto Ganymede's surface during the G1 flyby of Galileo, when the moon was located far above the center of Jupiter's magnetospheric current sheet. Panels (a) and (b) include precipitating electrons of all energies ($4.5 \text{ keV} \leq E \leq 100 \text{ MeV}$), while panels (c)–(h) display fluxes for (c, d) $4.5 \text{ keV} \leq E < 450 \text{ keV}$, (e, f) $450 \text{ keV} \leq E < 40 \text{ MeV}$, and (g, h) $40 \text{ MeV} \leq E \leq 100 \text{ MeV}$. Panels (i) and (j) display the fluxes from electrons of all energies when considering only the superposition of Ganymede's permanent and induced dipole with the Jovian magnetospheric background field (i.e., for the case *without* plasma interaction currents). White denotes regions of zero electron flux (and hence regions with no precipitation). The locations of Ganymede's leading (between 0°W and 180°W longitude) and trailing (from 180°W to 0°W) hemispheres are marked in the top two panels. See Figure 4 for further details.

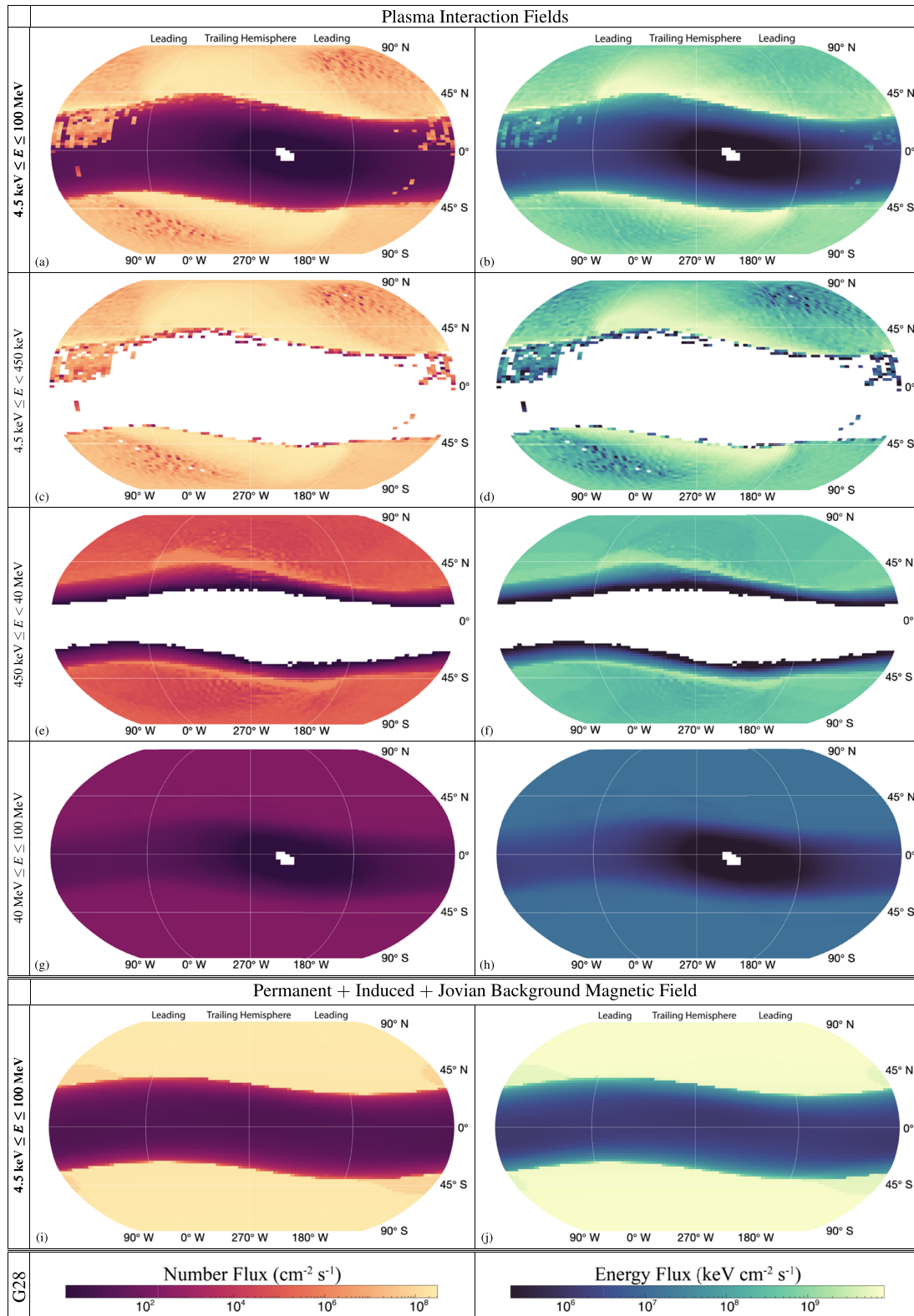


Figure 9. Energetic electron (left column) number and (right column) energy flux onto Ganymede's surface during the Galileo G28 encounter, when the moon was located far below the center of Jupiter's magnetospheric current sheet. The flux maps are separated by energy: (a, b) $4.5 \text{ keV} \leq E \leq 100 \text{ MeV}$, (c, d) $4.5 \text{ keV} \leq E < 450 \text{ keV}$, (e, f) $450 \text{ keV} \leq E < 40 \text{ MeV}$, and (g, h) $40 \text{ MeV} \leq E \leq 100 \text{ MeV}$. White colors denote regions of zero flux where no electron precipitation occurs. Panels (i) and (j) display the electron flux for the case *without* plasma interaction currents. See Figures 4 and 8 for further details.

left column in each of these figures shows the precipitating electron number flux, while the right column displays the energy flux. Again, Ganymede's orbital trailing (ramside) apex is centered in the figures, located at 270°W longitude, with the leading (wakeside) apex at 90°W along the two outer sides of each map. Identical to Figure 4, panels (a)–(h) in Figures 8 and 9 display the energetic electron flux maps when considering Ganymede's interaction with the thermal magnetospheric plasma (e.g., field line draping and compression of the minimagnetospheric field). Panels (i) and (j) in Figures 8 and 9, however, consider *only* the magnetic field generated by the superposition of Ganymede's permanent and induced magnetic moment with the local Jovian magnetospheric background field (i.e., *without* any contributions from Ganymede's perturbed electromagnetic environment).

The most striking difference between Figures 8 and 9 and the G8 flux maps is regions where *no* electrons are able to precipitate onto the surface, even at the highest energies of $E = 100$ MeV. This is most evident in the flux patterns during G1 visible in Figure 8, where an island of zero electron precipitation forms in the trailing hemisphere. This feature is centered near 270°W longitude within the “stripe” of reduced flux that already surrounds Ganymede's equator (see also Figure 4). A similar region inaccessible to energetic electrons is present for the G28 precipitation pattern (see Figure 9) but is much narrower in extent across the surface compared to during G1. The presence of these electron flux depletions is directly related to Ganymede's interaction with the ambient magnetospheric plasma during these two encounters. These features do not appear in the case without any plasma interaction currents; rather, the equatorial electron fluxes are homogeneous along the equator (see panels i and j in Figures 8 and 9).

Due to the reduced density of the ambient magnetospheric plasma outside of the Jovian current sheet compared to inside of it (see Bagenal & Delamere, 2011; Fatemi et al., 2016; Kivelson et al., 2004), Ganymede's minimagnetosphere was less compressed by the impinging plasma during the G1 and G28 encounters than it was during G8 (see also Jia et al., 2009). The magnetopause standoff distance was therefore farther from Ganymede's surface; the location where the magnetic field reverses from $B_z > 0$ within the minimagnetosphere to $B_z < 0$ outside of it was located farther upstream of the moon during G1 and G28. Hence, the “booster” region (where electrons experience a reduced magnetic field magnitude and their gyroradii increase; see Figure 6) was also located farther upstream during G1 and G28. In addition, the location of minimum $|B_z|$ associated with exiting Ganymede's minimagnetosphere corresponds to a much weaker minimum in $|\mathbf{B}|$ during these encounters compared to during G8, since the magnetospheric background field far above and below the center of Jupiter's magnetospheric current sheet had a strong nonzero B_y component. This “booster” effect was therefore much weaker during G1 and G28 than during G8. As a result, electrons *backtraced* from near 270°W longitude must travel farther upstream before reaching this region where enhanced gyroradii facilitate their escape from Ganymede's minimagnetosphere. Indeed, as visible in Figures 8 and 9, electrons at even the highest energy of $E = 100$ MeV are still unable to escape from near the apex of the trailing hemisphere. Instead, they return to Ganymede, intersect the surface, and become forbidden. Hence, a lens-like depletion in the energetic electron flux pattern forms near the moon's trailing apex during each of these encounters.

An additional feature in the G1 and G28 maps that was not present during G8 is a mottled flux pattern located at equatorial latitudes of the orbital leading hemisphere near 90°W. This pattern is driven by bombardment of electrons between approximately $4.5 \text{ keV} \leq E \leq 100 \text{ keV}$ (see Figures 8c and 8d, as well as Figures 9c and 9d). The majority of these electrons precipitate near the apex of the leading hemisphere, likely gaining access to Ganymede's minimagnetosphere via the downstream reconnection region. Since electrons drift counterclockwise around Ganymede after entering the minimagnetosphere, these features are slightly shifted into the sub-Jovian hemisphere toward 0°W (see especially Figure 9). Note that this feature does *not* appear in the electron patterns when Ganymede is embedded within the planetary current sheet (cf. the leading hemisphere fluxes during G8 in Figure 4) nor do they appear without including currents generated by Ganymede's thermal plasma interaction (cf. Figures 8h, 8i, 9h, and 9i). Hence, this mottled bombardment pattern is likely associated with the increased deformation of the moon's downstream magnetic environment when located outside of the Jovian magnetospheric current sheet (see, e.g., Fatemi et al., 2016; Jia et al., 2008; Paty & Winglee, 2004). Interestingly, however, Poppe et al. (2018) identified a similar feature in the energetic *ion* bombardment patterns during the G8 encounter (shifted rather toward 180°W due to an ion's clockwise sense of drift within Ganymede's field) and interpreted the mottled flux pattern in that region as indicating quasicontinuous precipitation onto the moon's midlatitude to low-latitude leading surface. These authors

did not investigate ion precipitation onto the moon while outside of Jupiter's current sheet, however, so it is unclear whether or not these features remain in the ion flux patterns over a full synodic period.

Despite the differences in the equatorial flux patterns with Ganymede located within the center of Jupiter's magnetospheric current sheet compared to above or below it, the fluxes onto the poles are largely the same, with an average number flux on the order of $10^8 \text{ cm}^{-2} \text{ s}^{-1}$ and an energy flux of approximately $10^9 \text{ keV cm}^{-2} \text{ s}^{-1}$. As during G8, the polar fluxes are markedly *not* homogeneous: Figures 8 and 9 display two “bands” of enhanced number and energy flux at latitudes poleward of approximately 30°N/S in the trailing hemisphere during G1 and G28 that exceed the flux onto the polar leading hemisphere by an order of magnitude. These features are again caused by a combination of two effects: in the trailing hemisphere, electrons just below the critical energy E_c precipitate slightly poleward of the OCFB (see also Figure 2), and Ganymede's perturbed electromagnetic environment causes electrons to preferentially bombard the trailing surface.

As with G8, an equatorial “stripe” of reduced electron flux forms during the G1 and G28 encounters with similar size. For each of the flybys, the latitudinal extent of this stripe is larger in the trailing hemisphere (approximately 70° in width) than in the leading hemisphere (approximately 50° wide). In comparison to G8, these “stripes” during G1 and G28 cover a smaller latitudinal range across Ganymede's surface; the reduced upstream plasma pressure and weaker plasma interaction during these two flybys caused the minimagnetosphere to be less compressed, shifting the OCFB in the trailing hemisphere equatorward. Without considering the effect of Ganymede's interaction with the thermal magnetospheric plasma on the electron bombardment patterns, a clear distinction in the flux patterns in latitude still forms. Figures 8h and 8i show that during G1, this boundary separating the equatorial “stripe” from the enhanced high-latitude flux is nearly constant in latitude. However, Figures 9h and 9i illustrate that this boundary during G28 is “wavier” in longitude across the surface, similar to during the G8 encounter. The orientation of the local magnetic field during these encounters (i.e., the superposition of Ganymede's induced and permanent field with the Jovian background field) directly affects the “waviness” of these regions.

When Ganymede is located above the center of the Jovian current sheet, the ambient magnetic field points southward and away from Jupiter (i.e., with a component along $-\hat{y}$ of the GphiO system; see Figure 1a). However during G1, Ganymede's (permanent plus induced) magnetic moment had a strong component along the $+\hat{y}$ direction (Jia et al., 2008). Hence, when ignoring currents generated by the thermal plasma interaction, the location on the moon's surface where the superposed magnetic field has no tangential component (i.e., where it is radial to the surface) occurs near the geographic poles. This causes the boundaries of the equatorial “stripe” to be nearly uniform with longitude across Ganymede's surface.

On the other hand, when Ganymede is below the center of the Jovian current sheet, the local magnetospheric field points southward and toward Jupiter (i.e., with a component along $+\hat{y}$; see Figure 1c). Since Ganymede's permanent dipole moment is tilted into the sub-Jovian hemisphere (Kivelson et al., 2002), the superposition of the moon's permanent and induced magnetic moment during G28 was still oriented toward Jupiter. Hence, the location on the surface where the magnetic field was nearly radial to the moon was tilted away from Jupiter in the northern hemisphere and toward Jupiter in the southern hemisphere (for further details, see Figure 1c or, e.g., Fatemi et al., 2016; Jia et al., 2008, 2009; McGrath et al., 2013). As a result, in the northern trailing hemisphere, the OCFB is rotated away from the equator near 0°W longitude and toward the equator near 180°W . In the southern trailing hemisphere, this shift in the OCFB is opposite. The resulting energetic electron bombardment follows this orientation of the surface magnetic field, thereby rotating the flux pattern in a clockwise direction around 270°W longitude and generating the “wavy” equatorial stripe of reduced electron flux visible in Figures 9h and 9i.

Note that over a full Jovian rotation, currents induced within Ganymede's subsurface ocean reduce the maximum latitudinal range covered by the OCFB (see, e.g., Figure 1 of Saur et al., 2015). Hence, the total “rocking angle” of the OCFB changes by approximately 4° in latitude across the surface over the 10.5 hr synodic period, compared to a nearly 10° excursion were the ocean not present. In addition, properties of Ganymede's interaction with the Jovian plasma that occur on shorter timescales (e.g., compression of the minimagnetospheric field upstream of the moon and reconnection in the downstream region) also affect the location of the OCFB (e.g., Duling et al., 2014; Jia et al., 2009; Musacchio et al., 2017; Saur et al., 2015). For this reason, the “waviness” of the energetic electron flux near the OCFB is reduced (though still present) when considering the effect of plasma interaction currents on the precipitation patterns. This is especially evident

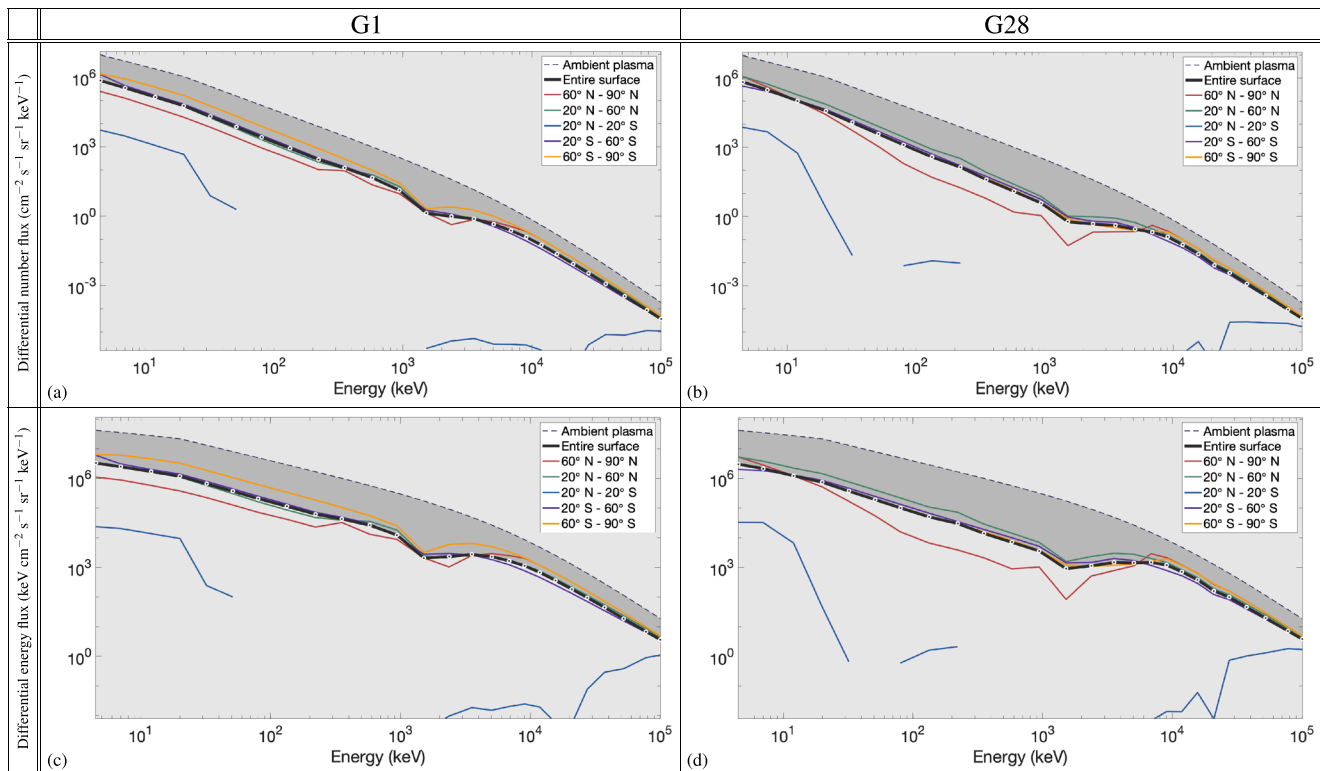


Figure 10. Average precipitating differential electron (a, b) number and (c, d) energy flux during the (left column) G1 and (right column) G28 flybys. Colors represent the same latitude bins as in Figure 7. Differential electron number and energy fluxes in the ambient plasma near Ganymede are represented by dashed lines, and shading denotes the difference between the ambient flux and the precipitating flux.

in Figure 9. For energetic particle observations obtained during close spacecraft encounters, a rotation of regions with enhanced electron precipitation by even a few degrees in latitude may cause asymmetries in measurements of electron intensities between inbound and outbound flyby segments. Such features have indeed been detected by the Galileo EPD during the polar G2 flyby of the moon, where the count rates obtained along the inbound segment of the flyby were higher than during the outbound portion (see Figure 1 of Williams et al., 1998).

Figure 10 displays the differential electron (a, b) number and (c, d) energy flux as a function of energy precipitating onto Ganymede for the (left column) G1 and (right column) G28 flybys. Colored lines represent separate latitude ranges across the surface, dashed lines denote the flux in the ambient plasma, and shading highlights the difference between the ambient and precipitating differential flux averaged over the entire surface. Similar to during the G8 encounter, Figure 10 shows that during G1 and G28, changes in the differential number flux span approximately 10 orders of magnitude between the lowest (4.5 keV) and highest (100 MeV) energies, while the energy flux spans nearly 6 orders of magnitude over this energy range. In addition, a slight depression in the fluxes again forms near the critical energy E_c , where the electrons' drift motion is in resonance with Ganymede's orbital velocity.

In contrast to G8, however, the flux of electrons with energies $4.5 \text{ keV} \leq E \leq 20 \text{ keV}$ is nonzero equatorward of 20° latitude during G1 and G28 (blue lines in Figure 10). This is a result of the mottled electron precipitation pattern from particles that enter Ganymede's minimagnetosphere from the downstream reconnection region and bombard the moon's leading surface, a mechanism that did not occur during G8 (cf. Figures 8 and 9 with Figure 4). However, electrons between energies of $50 \text{ keV} \leq E \leq 1.5 \text{ MeV}$ for G1 (see Figures 10a and 10c) and $200 \text{ keV} \leq E \leq 5 \text{ MeV}$ for G28 (see Figures 10b and 10d) are *not* able to penetrate the minimagnetosphere equatorward of 20° latitude. As a result, the equatorial differential flux approaches zero within these energy ranges. Such a dropout was not present during G8, where electrons above $E = 20 \text{ keV}$ were able to bombard the equatorial surface and contribute to nonzero fluxes. With increasing energy, electrons are again able to access equatorial latitudes during G1 and G28, but the fluxes remain below those during G8 until energies

above $E \approx 30$ MeV. Finally, even at the highest energy of $E = 100$ MeV, the apex of Ganymede's trailing hemisphere is still shielded from electron precipitation during G1 and G28 (see Figures 8 and 9), and the average equatorial fluxes remain nearly a factor of 5 below the flux of 100 MeV electrons averaged over the moon's surface. This decrease in the precipitating electron flux at the highest energies extends well beyond Ganymede's surface, reaching altitudes greater than 200 km (see Allieux et al., 2013).

In comparing the fluxes as a function of latitude displayed in Figure 10, an interesting difference between G1 (left column) and G28 (right column) is apparent. During G1, Ganymede's south polar cap (poleward of 60°S latitude) received more flux, on average, than the other four latitude ranges. This occurred, in part, because when Ganymede is located above the center of the Jovian current sheet (as was the case during G1), the azimuthal displacement $|r_{\text{eq}}|$ of an electron after mirroring in Jupiter's south polar hemisphere and returning to the moon is larger than $|r_{\text{eq}}|$ for its counterpart mirroring in the northern hemisphere (see Figure 2). Hence, a larger number of *backtraced* electrons initialized near the south pole have allowed trajectories compared to those initialized in the north, thereby resulting in a larger flux in the southern polar cap during G1. A similar pattern was present for the G8 encounter (see Figure 7), which occurred when Ganymede was slightly above the center of the current sheet.

During G28, Ganymede was located well below Jupiter's magnetospheric current sheet, and the difference in the azimuthal displacements for electrons returning to the moon after mirroring is reversed (an electron mirroring in Jupiter's northern hemisphere returns farther from the moon than its counterpart in the south). However, Figures 10b and 10d show that the north polar electron flux during G28 is reduced nearly an order of magnitude below the average flux elsewhere across the surface. Figure 9 illustrates that this is the result of a flux depletion that forms in Ganymede's northern leading hemisphere near 90°W longitude.

5.3. Time-Averaged Energetic Electron Precipitation Onto Ganymede

The flux maps in Figures 4, 8, and 9 correspond to the three “extremes” of Ganymede's location with respect to Jupiter's magnetospheric current sheet (*viz.*, far above the current sheet, embedded within the sheet, and far below it). Hence, in order to obtain a map of the *mean* energetic electron flux deposited onto Ganymede's surface during a full synodic rotation, we average the bombardment patterns during these three cases. The curves displayed in Figure 3 represent an average state of the ambient energetic electron population near Ganymede—each using data sets obtained over multiple years—and the resulting fits lie within a factor of approximately 8 from one another. We note that minor deviations from these averages occur on a flyby-to-flyby basis in the ambient energetic electron population. For example, the ambient number flux near Ganymede is around 3 times lower when the moon is located far outside of the Jovian current sheet compared to the ambient flux within it (e.g., Jun et al., 2005; Paranicas et al., 2018). However, during a full synodic rotation, Ganymede spends more at these large magnetic latitudes than it spends near the center of the current sheet (again differing by a factor of approximately 3; see, e.g., Figure 2 of Jia et al., 2008). In addition, transient magnetospheric “storms” may cause the local flux to be enhanced by nearly an order of magnitude (e.g., Roussos et al., 2018). Therefore, while it is likely that slight quantitative differences may arise in the resulting time-averaged energetic electron flux onto Ganymede's surface, the degree to which they are affected remains unknown. Regardless, the qualitative bombardment patterns will *not* be affected by the chosen fit from Figure 3 *nor* by such infrequent magnetospheric events.

Figure 11 displays the resulting time-averaged electron fluxes. Even in these mean flux maps, the effect of Ganymede's thermal plasma interaction on the energetic electrons is immediately evident. For example, fluxes in the trailing hemisphere poleward of the OCFB—which is shifted toward higher latitudes as the plasma interaction compresses the closed field line region—remain nearly an order of magnitude larger than in the polar leading hemisphere. Fluxes near the equator are inhomogeneous in longitude, with a region of minimum number flux (on the order of $10\text{ cm}^{-2}\text{ s}^{-1}$) carved out of the trailing, anti-Jovian hemisphere due to the presence of Ganymede's perturbed electromagnetic field environment. Hence, while individual small-scale flux patterns during the G1, G8, and G28 flybys have been averaged out (e.g., the region of zero electron precipitation surrounding Ganymede's trailing apex), the energy deposition patterns visible in Figure 11 likely persist over geologic timescales.

The distinct separation near the OCFB between the region of enhanced high-latitude electron flux and the region of reduced equatorial flux in Figure 11 can be compared to the observed location of Ganymede's bright polar caps (e.g., Smith et al., 1979). These disparate regions are clearly visible in Figure 3 of Khurana et al. (2007). The equatorial boundary of enhanced electron flux is in strong agreement with the high-latitude

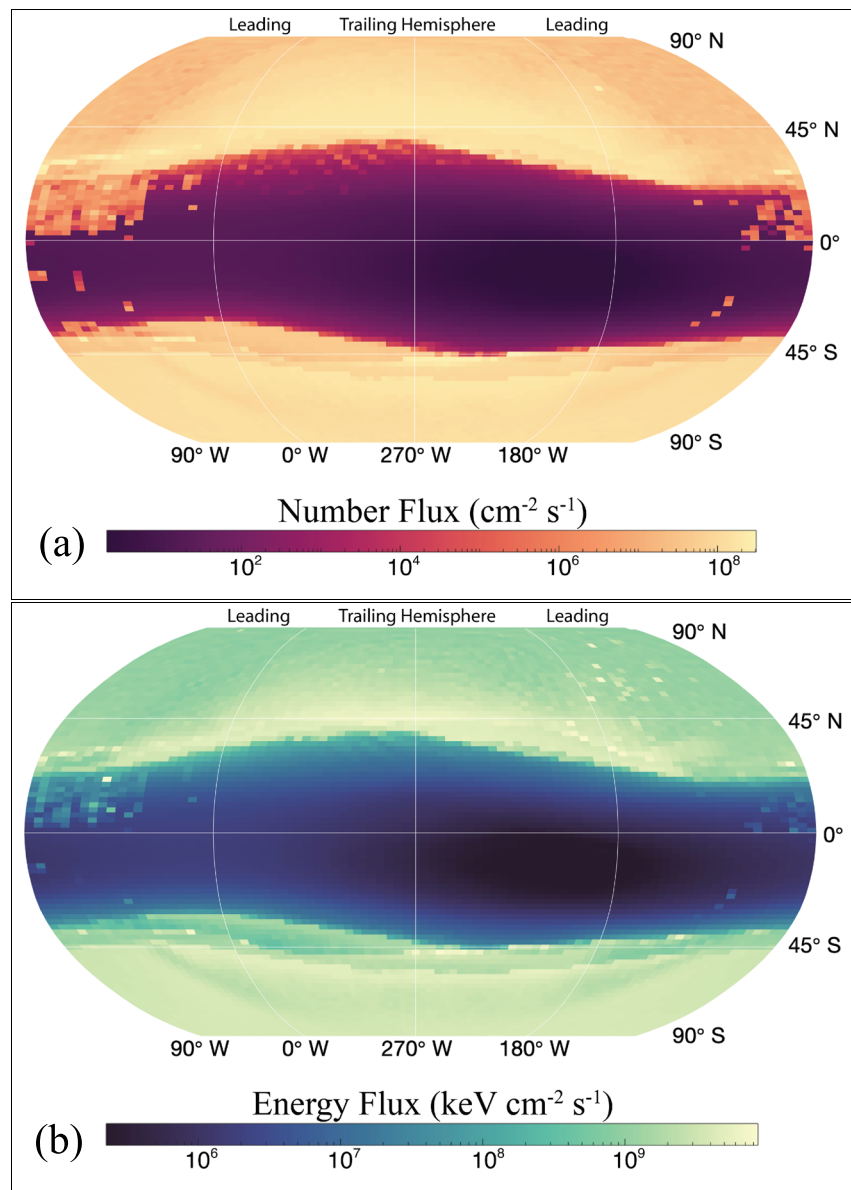


Figure 11. Energetic electron (a) number and (b) energy flux deposited onto Ganymede's surface averaged over a full Jovian synodic period.

brightness feature, especially from longitudes of 270°W extending well into the moon's sub-Jovian hemisphere. In the anti-Jovian, leading hemisphere, the location of enhanced flux appears to extend to more southern latitudes than in Figure 3 of Khurana et al. (2007). Similar agreement between these observed high-latitude brightness features has also been correlated with the precipitation of energetic ions onto Ganymede (see Fatemi et al., 2016; Poppe et al., 2018).

However, energetic electrons also amorphize low-temperature ices (Baragiola, 2003; Dubochet & Lepault, 1984; Loeffler et al., 2020), consistent with the observations of the amorphous (i.e., noncrystalline) state of Ganymede's polar surface (e.g., Hansen & McCord, 2004; Paranicas et al., 2018). Considering the dominance in both number and energy flux of energetic electrons into this region compared to ions (see Table 1), the high-latitude bombardment by these energetic electrons is likely a crucial process influencing the ice state of Ganymede's polar caps. At equatorial latitudes, the longitudinal asymmetry of the electron flux pattern visible in Figure 11 is consistent with the moon's observed equatorial albedo pattern, in which the orbital

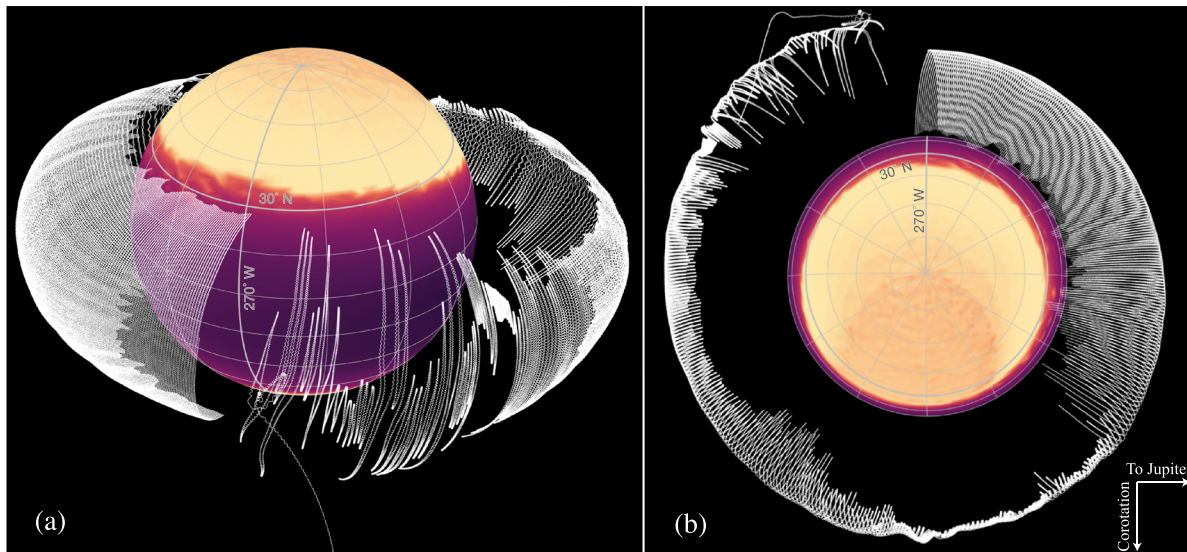


Figure 12. Trajectory of a *backtraced* 100 keV electron quasitrapped in Ganymede's minimagnetospheric field for the electromagnetic fields during the G8 encounter. This electron is initialized upstream of the moon in the equatorial plane at 270°W longitude, at an altitude of $0.6 R_G$ above the moon's trailing apex. The trajectory is viewed from a location (a) upstream of Ganymede in its northern, anti-Jovian hemisphere and (b) above the moon's geographic north pole. Projected onto Ganymede's surface is the energetic electron number flux during G8 from Figure 4a, with an identical color scale.

leading hemisphere is brighter than the trailing hemisphere (see also Khurana et al., 2007). Indeed, the abundance of a surface “darkening agent” at equatorial latitudes centered in Ganymede's trailing, anti-Jovian hemisphere has recently been detected (Ligier et al., 2019), the distribution of which is well correlated with the reduced energetic electron flux onto this region between 180°W and 270°W longitude (see Figure 11). Hence, over large timescales, energetic electron bombardment (or lack thereof) likely plays an important role in the generation of these equatorial surface patterns.

In addition to the correlation between energetic electron bombardment patterns and features observed on Ganymede's surface, these particles likely alter the moon's subsurface. The energy deposited into ice at depths below several micrometers is dominated by energetic electrons (e.g., Cooper et al., 2001); at energies above $E \approx 10$ MeV, electrons can reach depths greater than 10 cm, while ions do not penetrate below 0.1 cm (Hand & Carlson, 2011; Nordheim et al., 2018). Importantly, our findings have shown that Ganymede's magnetic field is *not* able to shield the equatorial surface from electrons at energies $E \geq 40$ MeV to prevent precipitation throughout Ganymede's leading hemisphere. At even greater energies (especially above 100 MeV from, e.g., cosmic rays), Ganymede's magnetic field is insufficient in shielding electrons from bombarding *anywhere* on the surface. So, although the equatorial electron energy flux is reduced by nearly 2 orders of magnitude compared to that of energetic ions (see Table 1), the low-latitude surface is still battered by high-energy electrons with the first 10 cm of the ice layer likely irradiated, especially over geologic timescales. Finally at high latitudes, since electrons of *any* energy can precipitate poleward of the OCFB, it is also unlikely that unaltered material exists at depths shallower than approximately 10 cm within the moon's polar caps.

6. Future Outlook

Results from this study have shown that Ganymede's closed field line region effectively shields the equatorial surface from precipitation of magnetospheric electrons below energies of $E \approx 40$ MeV. At altitudes above the surface, however, Galileo observations suggest a resident population of electrons at lower energies (between $15 \text{ keV} \lesssim E \lesssim 500 \text{ keV}$) trapped within the closed field line region of the minimagnetospheric field (Williams, 2004; Williams et al., 1997). To investigate this trapped population, Allieux et al. (2013) modeled Ganymede's magnetic environment using an analytical superposition of the moon's permanent field with the local Jovian background field and studied the two-dimensional evolution of energetic electron trajectories near the moon in the plane containing the direction of corotation and Ganymede's spin axis. Allieux et al. (2013) found that electrons with energies $E \leq 30$ MeV bounce within the closed field line region of

Ganymede's field for at least five bounce periods, after which those authors considered the electrons to be trapped and stopped tracing the particles. However, due to the rapid bounce motion of these electrons, it is likely that they remain trapped over much longer timescales.

Figure 12 displays the orbit of one such quasitrapped electron around Ganymede. In order to identify the location from which this electron approached Ganymede to become trapped, this particle is initialized with an energy of $E = 100$ keV at an altitude of $0.6 R_G$ above the moon's trailing apex and is traced *backward* in time using GENTOO while exposed to the electromagnetic fields during the G8 flyby. Figure 12a is viewed from a location upstream of Ganymede in the moon's northern, anti-Jovian hemisphere, while Figure 12b is viewed from above the geographic north pole. During its bounce motion along the closed field lines, this quasitrapped electron travels around the moon in a clockwise direction (when viewed from above in the backtracing approach; see Figure 12b). During its excursion through the minimagnetosphere, the electron's trajectory effectively highlights the magnetic field line topology; namely, compression of the field lines by Ganymede's interaction with the thermal magnetospheric plasma pushes the OCFB poleward in the trailing hemisphere, while this boundary is dragged equatorward in the leading hemisphere. Energetic electron observations from the Galileo EPD indeed suggest similar electron paths through this field line geometry (see Williams et al., 1998). The *backtraced* electron returns to near 270° W longitude after approximately 60 s (compared to its gyroperiod on the order of 10^{-5} s), when it then leaves Ganymede's local environment, traveling southward out of Jupiter's equatorial plane.

In a forward-tracing scenario, the motion of this electron is consistent with Galileo observations of trapped electron butterfly distributions during close flybys of the moon. Williams et al. (1997) suggest that such distributions form as electrons with field-aligned trajectories enter Ganymede's minimagnetosphere at high latitudes, become scattered into the equatorial closed field line region, and subsequently drift about the moon. Those electrons whose pitch angles remain near 0° and 180° after becoming trapped in the local field impact Ganymede's surface during their bounce (at altitudes of $0.6 R_G$, the loss cone associated with Ganymede's permanent dipole field is approximately 25°). Electrons with pitch angles near 90° , on the other hand, experience magnetospheric shell-splitting effects (e.g., Roederer, 1967), travel outside of the minimagnetosphere, and are also lost. The resulting distribution observed by Galileo displays a characteristic butterfly shape. Indeed, the electron in Figure 12 approaches Ganymede along an open field line and displays the exact quasitrapped behavior postulated by Williams et al. (1997). However, multiple physical effects are yet to be constrained. For example, how these electrons become entrained in Ganymede's minimagnetospheric field and are scattered, the timescales during which the resulting quasitrapped trajectories remain stable, the efficiency of trapping as a function of electron energy, how Ganymede's induced field and plasma interaction may affect the evolution and stability of these electronic radiation belts, and the extent to which the resulting ring current influences the local minimagnetospheric magnetic field remain unknown. The understanding of these processes is the focus of future work.

7. Conclusions

This study has investigated the dynamics of Jovian energetic electrons near Ganymede and constrained the resulting precipitation patterns and fluxes onto the surface for three distinct locations of the moon with respect to the center of Jupiter's magnetospheric current sheet. Our key findings can be summarized as follows:

1. Energetic electron bombardment of Ganymede is remarkably inhomogeneous across the surface, and the resulting number and energy fluxes are strongly partitioned by latitude and longitude. In order to accurately constrain these fluxes, the effect of the inhomogeneous electromagnetic field perturbations generated by Ganymede's interaction with Jupiter's thermal magnetospheric plasma on energetic electron dynamics must be included.
2. Within Ganymede's polar region, electrons of all energies are able to travel along open field lines to bombard the high-latitude surface. The contribution to the number flux of charged particles into Ganymede's polar caps from energetic electrons exceeds the ion contribution by an order of magnitude. Since the energy flux onto Ganymede's poles is also dominated by precipitating electrons, it is likely that the high-latitude regions are strongly irradiated up to depths of approximately 10 cm.
3. The high-latitude electron precipitation patterns are *not* homogeneous. "Bands" of electron flux that are enhanced by over an order of magnitude compared to elsewhere at high latitudes form just poleward of

- the OCFB in the trailing hemisphere due to the rapid bounce motion of energetic electrons. In the leading hemisphere, the local fluxes are reduced below the polar average by nearly an order of magnitude. Such asymmetric precipitation patterns likely result in a nonuniform energy deposition into the surface.
4. When located near the center of Jupiter's magnetospheric current sheet, closed field lines surrounding Ganymede's equator shield electrons below energies of $E \approx 40$ MeV from precipitating onto the surface. However, the OCFB is not a sharp boundary to this latitudinal partition; with increasing energy, electrons are gradually able to access subsequently lower latitudes until they reach the equator.
 5. The equatorial flux resulting from precipitation of electrons at energies $E \geq 40$ MeV is comparable to the flux of individual energetic ion species, despite remaining nearly 2 orders of magnitude below the total energetic ion flux onto this region. However, since these high-energy electrons penetrate deep into ice and deposit their energy at greater depths than ions, it is likely that Ganymede's low-latitude surface—in addition to its high-latitude surface—is irradiated to depths on the order of 10 cm. These equatorial electron fluxes display a longitudinal asymmetry: due to an electron's sense of gyration and drift within Ganymede's minimagnetospheric field, fluxes are enhanced in the leading, sub-Jovian hemisphere compared to antipodal locations. At energies beyond $E > 100$ MeV, Ganymede's closed field line region provides little to no shielding of the equatorial surface (i.e., from electrons of extra-Jovian origin).
 6. Differences in Ganymede's perturbed electromagnetic environment as a function of the moon's distance to the center of the Jovian magnetospheric plasma sheet generate changes in the energetic electron precipitation pattern that are most noticeable equatorward of 20°N and 20°S latitude. When far above or below the center of Jupiter's magnetospheric current sheet, electrons between energies of $4.5\text{keV} \leq E \lesssim 100\text{keV}$ are able to gain access to the equatorial leading hemisphere by entering the downstream reconnection region. However, energetic magnetospheric electrons at any energy $E \leq 100$ MeV are shielded from precipitating onto the apex of Ganymede's trailing hemisphere.
 7. Patterns of energetic electron bombardment show promising agreement with observed brightness asymmetries of Ganymede's surface ices when averaging over a full synodic rotation. The equatorial leading hemisphere near Ganymede's trailing apex receives the least amount of electron irradiation over large timescales, whereas the largest equatorial fluxes are deposited near the leading apex in the sub-Jovian hemisphere. These features are well correlated with the observed leading/trailing asymmetries in the moon's equatorial brightness patterns. Additionally, these features are *anticorrelated* with the equatorial bombardment patterns of energetic ions. At high latitudes, the locations of the boundaries between Ganymede's bright polar caps and dark equatorial surface are in agreement with regions near the OCFB that are exposed to the largest energetic electron fluxes anywhere on the surface.

Data Availability Statement

Data products resulting from this study are available online (<https://doi.org/10.5281/zenodo.3754987>).

Acknowledgments

L. L. and A. R. P. are supported by the National Aeronautics and Space Administration (NASA) Solar System Workings program, Grant NNX16AR99G. The work of S. S. is supported by state funds from the University System of Georgia, USA, and by NASA Grant 80NSSC20K0463. The authors thank Elias Roussos and an additional reviewer for their constructive comments on the original version of the manuscript. Special thanks are given to Kristen M. Thyng and Chad A. Greene for developing the perceptually uniform color scales used throughout this publication, which can be downloaded at matplotlib.org/cmocan (for further information and documentation of these color scales, see Thyng et al., 2016).

References

- Allioux, R., Louarn, P., & André, N. (2013). Model of energetic populations at Ganymede, implications for an orbiter. *Advances in Space Research*, *51*(7), 1204–1212. <https://doi.org/10.1016/j.asr.2012.10.033>
- Anderson, J. D., Lau, E. L., Sjogren, W. L., Schubert, G., & Moore, W. B. (1996). Gravitational constraints on the internal structure of Ganymede. *Nature*, *384*(6609), 541–543. <https://doi.org/10.1038/384541a0>
- Arnold, H., Liuzzo, L., & Simon, S. (2019). Magnetic signatures of a plume at Europa during the Galileo E26 flyby. *Geophysical Research Letters*, *46*, 1149–1157. <https://doi.org/10.1029/2018GL081544>
- Arnold, H., Liuzzo, L., & Simon, S. (2020). Plasma interaction signatures of plumes at Europa. *Journal of Geophysical Research: Space Physics*, *125*, e2019JA027346. <https://doi.org/10.1029/2019JA027346>
- Bagenal, F., & Delamere, P. A. (2011). Flow of mass and energy in the magnetospheres of Jupiter and Saturn. *Journal of Geophysical Research*, *116*, A05209. <https://doi.org/10.1029/2010JA016294>
- Bagenal, F., Wilson, R. J., Siler, S., Paterson, W. R., & Kurth, W. S. (2016). Survey of Galileo plasma observations in Jupiter's plasma sheet. *Journal of Geophysical Research: Planets*, *121*, 871–894. <https://doi.org/10.1002/2016JE005009>
- Baragiola, R. A. (2003). Water ice on outer solar system surfaces: Basic properties and radiation effects. *Planetary and Space Science*, *51*(14–15), 953–961. <https://doi.org/10.1016/j.pss.2003.05.007>
- Belcher, J. W. (1983). The low-energy plasma in the Jovian magnetosphere. *Physics of the Jovian Magnetosphere*, *1*, 68–105.
- Breer, B. R., Liuzzo, L., Arnold, H., Andersson, P. N., & Simon, S. (2019). Energetic ion dynamics in the perturbed electromagnetic fields near Europa. *Journal of Geophysical Research: Space Physics*, *124*, 7592–7613. <https://doi.org/10.1029/2019JA027147>
- Brice, N., & McDonough, R. (1973). Jupiter's radiation belts. *Icarus*, *18*, 206–219.
- Calvin, W. M., & Spencer, J. R. (1997). Latitudinal distribution of O₂ on Ganymede: Observations with the Hubble Space Telescope. *Icarus*, *130*(2), 505–516. <https://doi.org/10.1006/icar.1997.5842>
- Carnielli, G., Galand, M., Leblanc, F., Leclercq, L., Modolo, R., Beth, A., et al. (2019). First 3D test particle model of Ganymede's ionosphere. *Icarus*, *330*(October 2017), 42–59. <https://doi.org/10.1016/j.icarus.2019.04.016>

- Carnielli, G., Galand, M., Leblanc, F., Modolo, R., Beth, A., & Jia, X. (2020). Simulations of ion sputtering at Ganymede. *Icarus*, 351(August 2019), 113,918. <https://doi.org/10.1016/j.icarus.2020.113918>
- Clarke, J. T., Ajello, J., Ballester, G., Jaffel, L. B., Connerney, J., Gérard, J. C., et al. (2002). Ultraviolet emissions from the magnetic footprints of Io, Ganymede and Europa on Jupiter. *Nature*, 415(6875), 997–1000. <https://doi.org/10.1038/415997a>
- Connerney, J. E. P., Acuña, M. H., Ness, N. F., & Satoh, T. (1998). New models of Jupiter's magnetic field constrained by the Io flux tube footprint. *Journal of Geophysical Research*, 103(A6), 11,929–11,939. <https://doi.org/10.1029/97JA03726>
- Cooper, J. F., Johnson, R. E., Mauk, B. H., Garrett, H. B., & Gehrels, N. (2001). Energetic ion and electron irradiation of the icy Galilean satellites. *Icarus*, 149(1), 133–159. <https://doi.org/10.1006/icar.2000.6498>
- Dalton, J. B., Cassidy, T., Paranicas, C., Shirley, J. H., Prockter, L. M., & Kamp, L. W. (2013). Exogenic controls on sulfuric acid hydrate production at the surface of Europa. *Planetary and Space Science*, 77, 45–63. <https://doi.org/10.1016/j.pss.2012.05.013>
- de Pater, I., & Dunn, D. E. (2003). VLA observations of Jupiter's synchrotron radiation at 15 and 22 GHz. *Icarus*, 163(2), 449–455. [https://doi.org/10.1016/S0019-1035\(03\)00068-X](https://doi.org/10.1016/S0019-1035(03)00068-X)
- de Soria-Santacruz, M., Garrett, H. B., Evans, R. W., Jun, I., Kim, W., Paranicas, C., & Drozdov, A. (2016). An empirical model of the high-energy electron environment at Jupiter. *Journal of Geophysical Research: Space Physics*, 121, 9732–9743. <https://doi.org/10.1002/2016JA023059>
- Delitsky, M. L., & Lane, A. L. (1998). Ice chemistry on the Galilean satellites. *Journal of Geophysical Research*, 103(E13), 31,391–31,403. <https://doi.org/10.1029/1998JE900020>
- Divine, N., & Garrett, H. B. (1983). Charged particle distributions in Jupiter's magnetosphere. *Journal of Geophysical Research*, 88(A9), 6889–6903. <https://doi.org/10.1029/JA088iA09p06889>
- Dorelli, J. C., Gloer, A., Collinson, G., & Tóth, G. (2015). The role of the Hall effect in the global structure and dynamics of planetary magnetospheres: Ganymede as a case study. *Journal of Geophysical Research: Space Physics*, 120, 5377–5392. <https://doi.org/10.1002/2014JA020951>
- Dubochet, J., & Lepault, J. (1984). Cryo-electron microscopy of vitrified water. *Le Journal de Physique Colloques*, 45(C7), 7–85. <https://doi.org/10.1051/jphyscol:1984709>
- Duling, S., Saur, J., & Wicht, J. (2014). Consistent boundary conditions at nonconducting surfaces of planetary bodies: Applications in a new Ganymede MHD model. *Journal of Geophysical Research: Space Physics*, 119, 4412–4440. <https://doi.org/10.1002/2013JA019554>
- Erdman, P., & Zipf, E. (1986). Electron impact excitation of the O I λ 1172.6 Å multiplet. *Planetary and Space Science*, 34(11), 1155–1158. [https://doi.org/10.1016/0032-0633\(86\)90028-0](https://doi.org/10.1016/0032-0633(86)90028-0)
- Eviatar, A., Strobel, D. F., Wolven, B. C., Feldman, P. D., McGrath, M. A., & Williams, D. J. (2001). Excitation of the Ganymede ultraviolet aurora. *The Astrophysical Journal*, 555(2), 1013. <https://doi.org/10.1086/321510>
- Fatemi, S., Holmström, M., & Futaana, Y. (2012). The effects of lunar surface plasma absorption and solar wind temperature anisotropies on the solar wind proton velocity space distributions in the low-altitude lunar plasma wake. *Journal of Geophysical Research*, 117, A10105. <https://doi.org/10.1029/2011JA017353>
- Fatemi, S., Poppe, A. R., Khurana, K. K., Holmström, M., & Delory, G. T. (2016). On the formation of Ganymede's surface brightness asymmetries: Kinetic simulations of Ganymede's magnetosphere. *Geophysical Research Letters*, 43, 4745–4754. <https://doi.org/10.1002/2016GL068363>
- Feldman, P. D., McGrath, M. A., Strobel, D. F., Moos, H. W., Retherford, K. D., & Wolven, B. C. (2000). HST/STIS ultraviolet imaging of polar aurora on Ganymede. *The Astrophysical Journal*, 535(2), 1085–1090. <https://doi.org/10.1086/308889>
- Feyerabend, M., Simon, S., Motschmann, U., & Liuzzo, L. (2015). Filamented ion tail structures at Titan: A hybrid simulation study. *Planetary and Space Science*, 117, 362–376. <https://doi.org/10.1016/j.pss.2015.07.008>
- Frank, L. A., Paterson, W. R., Ackerson, K. L., & Bolton, S. J. (1997). Low-energy electron measurements at Ganymede with the Galileo spacecraft: Probes of the magnetic topology. *Geophysical Research Letters*, 24(17), 2159–2162. <https://doi.org/10.1029/97GL01632>
- Garrett, H. B., Jun, I., Ratliff, J. M., Evans, R. W., Clough, G. A., & McEntire, R. W. (2003). Galileo interim radiation electron (GIRE) model. JPL Publication, 03–006.
- Garrett, H. B., Kokorowski, M., & Jun, I. (2012). Galileo interim radiation electron model update—2012. JPL Publication, March 1–70.
- Gurnett, D. A., Kurth, W. S., Roux, A., Bolton, S. J., & Kennel, C. F. (1996). Evidence for a magnetosphere at Ganymede from plasma-wave observations by the Galileo spacecraft. *Nature*, 384(6609), 535–537. <https://doi.org/10.1038/384535a0>
- Hall, D. T., Feldman, P. D., McGrath, M. A., & Strobel, D. F. (1998). The far-ultraviolet oxygen airglow of Europa and Ganymede. *The Astrophysical Journal*, 499(1), 475–481. <https://doi.org/10.1086/305604>
- Hand, K. P., & Carlson, R. W. (2011). H₂O₂ production by high-energy electrons on icy satellites as a function of surface temperature and electron flux. *Icarus*, 215(1), 226–233. <https://doi.org/10.1016/j.icarus.2011.06.031>
- Hansen, G. B., & McCord, T. B. (2004). Amorphous and crystalline ice on the Galilean satellites: A balance between thermal and radiolytic processes. *Journal of Geophysical Research*, 109, E01012. <https://doi.org/10.1029/2003JE002149>
- Hill, T. W. (1979). Inertial limit on corotation. *Journal of Geophysical Research*, 84(A11), 6554–6558. <https://doi.org/10.1029/JA084iA11p06554>
- Howett, C., Spencer, J., Hurford, T., Verbiscer, A., & Segura, M. (2012). PacMan returns: An electron-generated thermal anomaly on Tethys. *Icarus*, 221(2), 1084–1088. <https://doi.org/10.1016/j.icarus.2012.10.013>
- Howett, C., Spencer, J., & Nordheim, T. (2020). Bolometric bond albedo and thermal inertia maps of Mimas. *Icarus*, 348(March), 113,745. <https://doi.org/10.1016/j.icarus.2020.113745>
- Howett, C., Spencer, J., Schenk, P., Johnson, R., Paranicas, C., Hurford, T., et al. (2011). A high-amplitude thermal inertia anomaly of probable magnetospheric origin on Saturn's moon Mimas. *Icarus*, 216(1), 221–226. <https://doi.org/10.1016/j.icarus.2011.09.007>
- Ip, W. H. H., Williams, D. J., McEntire, R. W., & Mauk, B. (1997). Energetic ion sputtering effects at Ganymede. *Geophysical Research Letters*, 24(21), 2631–2634. <https://doi.org/10.1029/97GL02814>
- Jia, X., Walker, R. J., Kivelson, M. G., Khurana, K. K., & Linker, J. A. (2008). Three-dimensional MHD simulations of Ganymede's magnetosphere. *Journal of Geophysical Research*, 113, A06212. <https://doi.org/10.1029/2007JA012748>
- Jia, X., Walker, R. J., Kivelson, M. G., Khurana, K. K., & Linker, J. A. (2009). Properties of Ganymede's magnetosphere inferred from improved three-dimensional MHD simulations. *Journal of Geophysical Research*, 114, A09209. <https://doi.org/10.1029/2009JA014375>
- Johnson, R., Carlson, R., Cooper, J., Paranicas, C., Moore, M., & Wong, M. (2004). Radiation effects on the surfaces of the Galilean satellites. *Jupiter: The Planet, Satellites and Magnetosphere*, 51(7), 483–510.
- Johnson, R., & Quickenden, T. (1997). Photolysis and radiolysis of water ice on outer solar system bodies. *Journal of Geophysical Research*, 102(E5), 10,985–10,996. <https://doi.org/10.1029/97JE00068>
- Joy, S. P., Kivelson, M. G., Walker, R. J., Khurana, K. K., Russell, C. T., & Ogino, T. (2002). Probabilistic models of the Jovian magnetopause and bow shock locations. *Journal of Geophysical Research*, 107(A10), 1309. <https://doi.org/10.1029/2001JA009146>

- Jun, I., Garrett, H. B., Cassidy, T. A., Kim, W., & Dougherty, L. (2019). Updating the Jovian electron plasma environment. *IEEE Transactions on Plasma Science*, *47*(8), 3915–3922. <https://doi.org/10.1109/TPS.2019.2901681>
- Jun, I., Garrett, H. B., Swimm, R., Evans, R. W., & Clough, G. (2005). Statistics of the variations of the high-energy electron population between 7 and 28 Jovian radii as measured by the Galileo spacecraft. *Icarus*, *178*(2), 386–394. <https://doi.org/10.1016/j.icarus.2005.01.022>
- Khurana, K. (1997). Euler potential models of Jupiter's magnetospheric field. *Journal of Geophysical Research*, *102*(A6), 11,295–11,306. <https://doi.org/10.1029/97JA00563>
- Khurana, K., Pappalardo, R., Murphy, N., & Denk, T. (2007). The origin of Ganymede's polar caps. *Icarus*, *191*(1), 193–202. <https://doi.org/10.1016/j.icarus.2007.04.022>
- Khurana, K., Russell, C., & Dougherty, M. (2008). Magnetic portraits of Tethys and Rhea. *Icarus*, *193*(2), 465–474. <https://doi.org/10.1016/j.icarus.2007.08.005>
- Kimura, J., Nakagawa, T., & Kurita, K. (2009). Size and compositional constraints of Ganymede's metallic core for driving an active dynamo. *Icarus*, *202*(1), 216–224. <https://doi.org/10.1016/j.icarus.2009.02.026>
- Kivelson, M., Bagenal, F., Kurth, W., Neubauer, F., Paranicas, C., & Saur, J. (2004). Magnetospheric interactions with satellites, *Jupiter: The planet, satellites and magnetosphere* (pp. 513–536). Cambridge, UK: Cambridge University Press.
- Kivelson, M., Khurana, K. K., Russell, C. T., Walker, R. J., Warnecke, J., Coroniti, F. V., et al. (1996). Discovery of Ganymede's magnetic field by the Galileo spacecraft. *Nature*, *384*(6609), 537–541. <https://doi.org/10.1038/384537a0>
- Kivelson, M., Khurana, K., & Volwerk, M. (2002). The permanent and inductive magnetic moments of Ganymede. *Icarus*, *157*(2), 507–522. <https://doi.org/10.1006/icar.2002.6834>
- Kollmann, P., Roussos, E., Paranicas, C., Woodfield, E. E., Mauk, B. H., Clark, G., et al. (2018). Electron acceleration to MeV energies at Jupiter and Saturn. *Journal of Geophysical Research: Space Physics*, *123*, 9110–9129. <https://doi.org/10.1029/2018JA025665>
- Kotova, A., Roussos, E., Krupp, N., & Dandouras, I. (2015). Modeling of the energetic ion observations in the vicinity of Rhea and Dione. *Icarus*, *258*, 402–417. <https://doi.org/10.1016/j.icarus.2015.06.031>
- Krupp, N., Kotova, A., Roussos, E., Simon, S., Liuzzo, L., Paranicas, C., et al. (2020). Magnetospheric interactions of Saturn's moon Dione (2005–2015). *Journal of Geophysical Research: Space Physics*, *125*, e27688. <https://doi.org/10.1029/2019JA027688>
- Krupp, N., Roussos, E., Krieger, H., Kollmann, P., Kivelson, M. G., Kotova, A., et al. (2013). Energetic particle measurements in the vicinity of Dione during the three Cassini encounters 2005–2011. *Icarus*, *226*(1), 617–628. <https://doi.org/10.1016/j.icarus.2013.06.007>
- Krupp, N., Roussos, E., Lagg, A., Woch, J., Müller, A. L., Krimigis, S. M., et al. (2009). Energetic particles in Saturn's magnetosphere during the Cassini nominal mission (July 2004–July 2008). *Planetary and Space Science*, *57*(14–15), 1754–1768. <https://doi.org/10.1016/j.pss.2009.06.010>
- Ligier, N., Paranicas, C., Carter, J., Poulet, F., Calvin, W., Nordheim, T., et al. (2019). Surface composition and properties of Ganymede: Updates from ground-based observations with the near-infrared imaging spectrometer SINFONI/VLT/ESO. *Icarus*, *333*(June), 496–515. <https://doi.org/10.1016/j.icarus.2019.06.013>
- Liuzzo, L., Simon, S., & Feyerabend, M. (2018). Observability of Callisto's inductive signature during the JUPITER ICy Moons Explorer mission. *Journal of Geophysical Research: Space Physics*, *123*, 9045–9054. <https://doi.org/10.1029/2018JA025951>
- Liuzzo, L., Simon, S., & Regoli, L. (2019a). Energetic electron dynamics near Callisto. *Planetary and Space Science*, *179*(August), 104726. <https://doi.org/10.1016/j.pss.2019.104726>
- Liuzzo, L., Simon, S., & Regoli, L. (2019b). Energetic ion dynamics near Callisto. *Planetary and Space Science*, *166*, 23–53. <https://doi.org/10.1016/j.pss.2018.07.014>
- Loeffler, M. J., Tribbett, P. D., Cooper, J. F., & Sturmer, S. J. (2020). A possible explanation for the presence of crystalline H₂O-ice on Kuiper Belt objects. *Icarus*, *351*, 113,943. <https://doi.org/10.1016/j.icarus.2020.113943>
- Mahjoub, A., Poston, M. J., Hand, K. P., Brown, M. E., Hodyss, R., Blacksberg, J., et al. (2016). Electron irradiation and thermal processing of mixed-ices of potential relevance to Jupiter Trojan asteroids. *The Astrophysical Journal*, *820*(2), 141. <https://doi.org/10.3847/0004‐637X/820/2/141>
- Mauk, B. H., Mitchell, D. G., McEntire, R. W., Paranicas, C. P., Roelof, E. C., Williams, D. J., et al. (2004). Energetic ion characteristics and neutral gas interactions in Jupiter's magnetosphere. *Journal of Geophysical Research*, *109*, A09S12. <https://doi.org/10.1029/2003JA010270>
- McGrath, M. A., Jia, X., Retherford, K., Feldman, P. D., Strobel, D. F., & Saur, J. (2013). Aurora on Ganymede. *Journal of Geophysical Research: Space Physics*, *118*, 2043–2054. <https://doi.org/10.1002/jgra.50122>
- Menietti, J. D., Shprits, Y. Y., Horne, R. B., Woodfield, E. E., Hospodarsky, G. B., & Gurnett, D. A. (2012). Chorus, ECH, and Z mode emissions observed at Jupiter and Saturn and possible electron acceleration. *Journal of Geophysical Research*, *117*, A12214. <https://doi.org/10.1029/2012JA018187>
- Musacchio, F., Saur, J., Roth, L., Retherford, K. D., McGrath, M. A., Feldman, P. D., & Strobel, D. F. (2017). Morphology of Ganymede's FUV auroral ovals. *Journal of Geophysical Research: Space Physics*, *122*, 2855–2876. <https://doi.org/10.1002/2016JA023220>
- Neubauer, F. (1998). The sub-Alfvénic interaction of the Galilean satellites with the Jovian magnetosphere. *Journal of Geophysical Research*, *103*, 843–866. <https://doi.org/10.1029/97JE03370>
- Noll, K. S., Johnson, R. E., Lane, A. L., Domingue, D. L., & Weaver, H. A. (1996). Detection of ozone on Ganymede. *Science*, *273*(5273), 341–343. <https://doi.org/10.1126/science.273.5273.341>
- Nordheim, T. A., Hand, K. P., & Paranicas, C. (2018). Preservation of potential biosignatures in the shallow subsurface of Europa. *Nature Astronomy*, *2*(8), 673–679. <https://doi.org/10.1038/s41550-018-0499-8>
- Nordheim, T. A., Hand, K. P., Paranicas, C., Howett, C. J., Hendrix, A. R., Jones, G. H., & Coates, A. J. (2017). The near-surface electron radiation environment of Saturn's moon Mimas. *Icarus*, *286*, 56–68. <https://doi.org/10.1016/j.icarus.2017.01.002>
- Nordheim, T. A., Jasinski, J. M., & Hand, K. P. (2019). Galactic cosmic-ray bombardment of Europa's surface. *The Astrophysical Journal*, *881*(2), L29. <https://doi.org/10.3847/2041-8213/ab3661>
- Paranicas, C., Carlson, R. W., & Johnson, R. E. (2001). Electron bombardment of Europa. *Geophysical Research Letters*, *28*(4), 673–676. <https://doi.org/10.1029/2000GL012320>
- Paranicas, C., Hibbitts, C. A., Kollmann, P., Ligier, N., Hendrix, A. R., Nordheim, T. A., et al. (2018). Magnetospheric considerations for solar system ice state. *Icarus*, *302*, 560–564. <https://doi.org/10.1016/j.icarus.2017.12.013>
- Paranicas, C., Paterson, W. R., Cheng, A. F., Mauk, B. H., McEntire, R. W., Frank, L. A., & Williams, D. J. (1999). Energetic particle observations near Ganymede. *Journal of Geophysical Research*, *104*(A8), 17,459–17,469. <https://doi.org/10.1029/1999ja900199>
- Paranicas, C., Roussos, E., Decker, R. B., Johnson, R. E., Hendrix, A. R., Schenk, P., et al. (2014). The lens feature on the inner Saturnian satellites. *Icarus*, *234*, 155–161. <https://doi.org/10.1016/j.icarus.2014.02.026>

- Patterson, G., Paranicas, C., & Prockter, L. (2012). Characterizing electron bombardment of Europa's surface by location and depth. *Icarus*, 220(1), 286–290. <https://doi.org/10.1016/j.icarus.2012.04.024>
- Paty, C., & Winglee, R. (2004). Multi-fluid simulations of Ganymede's magnetosphere. *Geophysical Research Letters*, 31, L24806. <https://doi.org/10.1029/2004GL021220>
- Paty, C., & Winglee, R. (2006). The role of ion cyclotron motion at Ganymede: Magnetic field morphology and magnetospheric dynamics. *Geophysical Research Letters*, 33, L10106. <https://doi.org/10.1029/2005GL025273>
- Payan, A. P., Paty, C. S., & Retherford, K. D. (2015). Uncovering local magnetospheric processes governing the morphology and variability of Ganymede's aurora using three-dimensional multifluid simulations of Ganymede's magnetosphere. *Journal of Geophysical Research: Space Physics*, 120, 401–413. <https://doi.org/10.1002/2014JA020301>
- Plainaki, C., Milillo, A., Massetti, S., Mura, A., Jia, X., Orsini, S., et al. (2015). The H₂O and O₂ exospheres of Ganymede: The result of a complex interaction between the Jovian magnetospheric ions and the icy moon. *Icarus*, 245, 306–319. <https://doi.org/10.1016/j.icarus.2014.09.018>
- Poppe, A. R., Fatemi, S., & Khurana, K. K. (2018). Thermal and energetic ion dynamics in Ganymede's magnetosphere. *Journal of Geophysical Research: Space Physics*, 123, 4614–4637. <https://doi.org/10.1029/2018JA025312>
- Regoli, L. H., Roussos, E., Feyerabend, M., Jones, G. H., Krupp, N., Coates, A. J., et al. (2016). Access of energetic particles to Titan's exobase: A study of Cassini's T9 flyby. *Planetary and Space Science*, 130, 40–53. <https://doi.org/10.1016/j.pss.2015.11.013>
- Roederer, J. G. (1967). On the adiabatic motion of energetic particles in a model magnetosphere. *Journal of Geophysical Research*, 72(3), 981–992. <https://doi.org/10.1029/jz072i003p00981>
- Roussos, E., Andriopoulou, M., Krupp, N., Kotova, A., Paranicas, C., Krimigis, S. M., & Mitchell, D. G. (2013). Numerical simulation of energetic electron microsignature drifts at Saturn: Methods and applications. *Icarus*, 226(2), 1595–1611. <https://doi.org/10.1016/j.icarus.2013.08.023>
- Roussos, E., Kollmann, P., Krupp, N., Paranicas, C., Dialynas, K., Sergis, N., et al. (2018). Drift-resonant, relativistic electron acceleration at the outer planets: Insights from the response of Saturn's radiation belts to magnetospheric storms. *Icarus*, 305, 160–173. <https://doi.org/10.1016/j.icarus.2018.01.016>
- Saur, J., Duling, S., Roth, L., Jia, X., Strobel, D. F., Feldman, P. D., et al. (2015). The search for a subsurface ocean in Ganymede with Hubble Space Telescope observations of its auroral ovals. *Journal of Geophysical Research: Space Physics*, 120, 1715–1737. <https://doi.org/10.1002/2014JA020778>
- Saur, J., Strobel, D. F., & Neubauer, F. M. (1998). Interaction of the Jovian magnetosphere with Europa: Constraints on the neutral atmosphere. *Journal of Geophysical Research*, 103(3339), 19,947–19,962. <https://doi.org/10.1029/97je03556>
- Schaible, M. J., Johnson, R. E., Zhigilei, L. V., & Piqueux, S. (2017). High energy electron sintering of icy regoliths: Formation of the PacMan thermal anomalies on the icy Saturnian moons. *Icarus*, 285, 211–223. <https://doi.org/10.1016/j.icarus.2016.08.033>
- Schubert, G., Zhang, K., Kivelson, M. G., & Anderson, J. D. (1996). The magnetic field and internal structure of Ganymede. *Nature*, 384(6609), 544–545. <https://doi.org/10.1038/384544a0>
- Schulz, M., & Lanzerotti, L. J. (2012). *Particle diffusion in the radiation belts* (Vol. 7). Springer Science & Business Media.
- Seufert, M., Saur, J., & Neubauer, F. M. (2011). Multi-frequency electromagnetic sounding of the Galilean moons. *Icarus*, 214(2), 477–494. <https://doi.org/10.1016/j.icarus.2011.03.017>
- Shprits, Y. Y., Menietti, J. D., Drozdov, A. Y., Horne, R. B., Woodfield, E. E., Groene, J. B., et al. (2018). Strong whistler mode waves observed in the vicinity of Jupiter's moons. *Nature Communications*, 9(1), 7–12. <https://doi.org/10.1038/s41467-018-05431-x>
- Smith, B. A., Soderblom, L. A., Beebe, R., Boyce, J., Briggs, G., Carr, M., et al. (1979). The Galilean satellites and Jupiter: Voyager 2 imaging science results. *Science*, 206(4421), 927–950. <https://doi.org/10.1126/science.206.4421.927>
- Sohl, F. (2002). Implications from Galileo observations on the interior structure and chemistry of the Galilean satellites. *International Journal of Solar System Studies*, 157, 104–119. <https://doi.org/10.1006/icar.2002.6828>
- Spencer, J. R., Calvin, W. M., & Person, M. J. (1995). Charge-coupled device spectra of the Galilean satellites: Molecular oxygen on Ganymede. *Journal of Geophysical Research*, 100(E9), 19,049. <https://doi.org/10.1029/95JE01503>
- Squyres, S. W. (1980). Surface temperatures and retention of H₂O frost on Ganymede and Callisto. *Icarus*, 44(2), 502–510. [https://doi.org/10.1016/0019-1035\(80\)90040-8](https://doi.org/10.1016/0019-1035(80)90040-8)
- Stormer, C. (1955). *The polar aurora*: Oxford: Clarendon Press.
- Szalay, J. R., Allegrini, F., Bagenal, F., Bolton, S. J., Bonfond, B., Clark, G., et al. (2020). Alfvénic acceleration sustains Ganymede's footprint tail aurora. *Geophysical Research Letters*, 47, e2019GL086527. <https://doi.org/10.1029/2019gl086527>
- Tóth, G., Jia, X., Markidis, S., Peng, I. B., Chen, Y., Daldorff, L. K. S., et al. (2016). Extended magnetohydrodynamics with embedded particle-in-cell simulation of Ganymede's magnetosphere. *Journal of Geophysical Research: Space Physics*, 121, 1273–1293. <https://doi.org/10.1002/2015JA021997>
- Teolis, B. D., Plainaki, C., Cassidy, T. A., & Raut, U. (2017). Water ice radiolytic O₂, H₂, and H₂O₂ yields for any projectile species, energy, or temperature: A model for icy astrophysical bodies. *Journal of Geophysical Research: Planets*, 122, 1996–2012. <https://doi.org/10.1002/2017JE005285>
- Thomsen, M. F., & Van Allen, J. A. (1980). Motion of trapped electrons and protons in Saturn's inner magnetosphere. *Journal of Geophysical Research*, 85(A11), 5831–5834. <https://doi.org/10.1029/JA085iA11p05831>
- Thyng, K., Greene, C., Hetland, R., Zimmerle, H., & DiMarco, S. (2016). True colors of oceanography: Guidelines for effective and accurate colormap selection. *Oceanography*, 29(3), 9–13. <https://doi.org/10.5670/oceanog.2016.66>
- Tripathi, A., Singhal, R., Singh, K., & Singh, O. (2014). Whistler mode instability and pitch-angle diffusion near Ganymede. *Planetary and Space Science*, 92, 150–156. <https://doi.org/10.1016/j.pss.2014.01.005>
- Truscott, P., Heynderickx, D., Sicard-Piet, A., & Bourdarie, S. (2011). Simulation of the radiation environment near Europa using the geant4-based PLANETOCOSMICS-J model. *IEEE Transactions on Nuclear Science*, 58(6 PART 1), 2776–2784. <https://doi.org/10.1109/TNS.2011.2172818>
- Vay, J. L. (2008). Simulation of beams or plasmas crossing at relativistic velocity. *Physics of Plasmas*, 15(5), 056,701. <https://doi.org/10.1063/1.2837054>
- Wang, L., Germaschewski, K., Hakim, A., Dong, C., Raeder, J., & Bhattacharjee, A. (2018). Electron physics in 3-D two-fluid 10-moment modeling of Ganymede's magnetosphere. *Journal of Geophysical Research: Space Physics*, 123, 2815–2830. <https://doi.org/10.1002/2017JA024761>
- Wells, W., Borst, W., & Zipf, E. (1971). Absolute cross section for the production of O(⁵S⁰) by electron impact dissociation of O₂. *Chemical Physics Letters*, 12(2), 288–290. [https://doi.org/10.1016/0009-2614\(71\)85066-2](https://doi.org/10.1016/0009-2614(71)85066-2)
- Williams, D. J. (2004). Energetic electron beams in Ganymede's magnetosphere. *Journal of Geophysical Research*, 109, A09211. <https://doi.org/10.1029/2004JA010521>

- Williams, D. J., & Mauk, B. (1997). Pitch angle diffusion at Jupiter's moon Ganymede. *Journal of Geophysical Research*, *102*(A11), 24,283–24,287. <https://doi.org/10.1029/97JA02260>
- Williams, D. J., Mauk, B., & McEntire, R. W. (1997). Trapped electrons in Ganymede's magnetic field. *Geophysical Research Letters*, *24*(23), 2953–2956. <https://doi.org/10.1029/97GL03003>
- Williams, D. J., Mauk, B., & McEntire, R. W. (1998). Properties of Ganymede's magnetosphere as revealed by energetic particle observations. *Journal of Geophysical Research*, *103*(A8), 17,523–17,534. <https://doi.org/10.1029/98JA01370>
- Wright, T. P., & Hadley, G. R. (1975). Relativistic distribution functions and applications to electron beams. *Physical Review A*, *12*(2), 686–697. <https://doi.org/10.1103/PhysRevA.12.686>
- Xiao, F., Shen, C., Wang, Y., Zheng, H., & Wang, S. (2008). Energetic electron distributions fitted with a relativistic kappa-type function at geosynchronous orbit. *Journal of Geophysical Research*, *113*, A05203. <https://doi.org/10.1029/2007JA012903>
- Zhang, H. (2003). Internal structure models and dynamical parameters of the Galilean satellites. *Celestial Mechanics and Dynamical Astronomy*, *87*(1–2), 189–195. <https://doi.org/10.1023/A:1026188029324>
- Zheng, W., Jewitt, D., & Kaiser, R. I. (2006). Formation of hydrogen, oxygen, and hydrogen peroxide in electron-irradiated crystalline water ice. *The Astrophysical Journal*, *639*(1), 534–548. <https://doi.org/10.1086/499231>
- Zhou, H., Tóth, G., Jia, X., Chen, Y., & Markidis, S. (2019). Embedded kinetic simulation of Ganymede's magnetosphere: Improvements and inferences. *Journal of Geophysical Research: Space Physics*, *124*, 5441–5460. <https://doi.org/10.1029/2019JA026643>